IOWA STATE UNIVERSITY
Digital Repository

Graduate Theses and Dissertations

Iowa State University Capstones, Theses and Dissertations

2009

Engine spray combustion modeling using unified spray model with dynamic mesh refinement

Ravi Kolakaluri
Iowa State University

Follow this and additional works at: https://lib.dr.iastate.edu/etd

 Part of the Mechanical Engineering Commons

Recommended Citation
Kolakaluri, Ravi, "Engine spray combustion modeling using unified spray model with dynamic mesh refinement" (2009). *Graduate Theses and Dissertations*. 10769.
https://lib.dr.iastate.edu/etd/10769

This Thesis is brought to you for free and open access by the Iowa State University Capstones, Theses and Dissertations at Iowa State University Digital Repository. It has been accepted for inclusion in Graduate Theses and Dissertations by an authorized administrator of Iowa State University Digital Repository. For more information, please contact digirep@iastate.edu.

www.manaraa.com

Engine spray combustion modeling using unified spray model with dynamic mesh refinement

by

Ravi Kolakaluri

A thesis submitted to the graduate faculty

In partial fulfillment of the requirements for the degree of

MASTER OF SCIENCE

Major: Mechanical Engineering

Program of Study Committee:

Song Charng Kong (Major Professor)

Shankar Subramaniam

LeAnn Faidley

Iowa State University

Ames, Iowa

2009

Copyright © Ravi Kolakaluri, 2009. All rights reserved.

www.manaraa.com

TABLE OF CONTENTS

Page

www.manaraa.com

www.manaraa.com

ABSTRACT

The primary objective of this study is to improve the spray and combustion modeling of internal combustion engines using dynamic mesh refinement. The first part of the study used advanced spray models with a dynamic mesh refinement scheme to simulate atomization of gasoline and diesel sprays. Traditionally gasoline sprays and diesel sprays were simulated using different models due to their different characteristics. This study was able to use the same set of models without adjustments in model constants and obtain good agreement between experimental and simulation results. The model was also used to simulate a direct-injection gasoline engine with realistic geometry. The present spray model with dynamic mesh refinement algorithm was shown to predict the spray structure and liquid penetration accurately with reasonable computational cost.

In the second part of this study, diesel combustion modeling was performed using the above advanced spray model. The Shell ignition model, which uses a simplified reaction mechanism, was used to simulate the autoignition process of hydrocarbon fuels. The laminar-and-turbulent characteristic-time combustion model along with the Shell model was used to simulate the overall low and high temperature chemistry. The simulation results were compared with the experimental data with good agreement. The combination of combustion and spray models along with the dynamic mesh refinement was also validated using experimental data obtained from a heavy-duty diesel engine. In conclusion, a model, which is a combination of advanced spray model and combustion model with dynamic mesh refinement, was developed to simulate spray combustion in internal combustion engines.

www.manaraa.com

ACKNOWLEDGEMENT

Foremost, I would like to express my sincere gratitude to my advisor Prof. Song-Charng Kong for the continuous support of my MS study and research, for his patience, motivation, enthusiasm, and knowledge. His guidance helped me with the research and writing of this thesis. This thesis would not have been possible without his guidance. In addition, he was always accessible and willing to help his students with their research.

Besides my advisor, I would like to thank the rest of my thesis committee, Prof. Shankar Subramaniam and Prof. LeAnn Faidley for being in my committee.

My deepest gratitude goes to my family for their unflagging love and support throughout my life, especially to my mother for her prayers and support.

I thank my fellow labmates in Computational Fluid Dynamics lab for the support and all the fun we had in the last two years.

Last but not least, thanks be to God for my life through all tests. You have made my life more bountiful. May your name be exalted, honored, and glorified.

www.manaraa.com

LIST OF TABLES

www.manaraa.com

LIST OF FIGURES

www.manaraa.com

www.manaraa.com

www.manaraa.com

www.manaraa.com

CHAPTER 1. INTRODUCTION

1.1 Motivation

With the rising competition in engine industry and emission restrictions due to the environmental concerns, manufacturers are forced to explore cost-effective ways to evaluate engine performance using different combustion chamber geometries, fuel injection strategies, combustion processes and alternative fuels. The fuel consumption and emissions can be reduced by improving the fuel injection system and the combustion process.

Despite the uncertainties of numerical simulation often greater than those of experiments, the modeling of spray and combustion process has some significant advantages. The numerical simulations are especially suited to carry out extensive parametric studies in more time and cost effective way compared to experiments. The numerical simulations also allow to output very single variable of a problem at any position in physical space and at any point in time during the process. Such a complete set of information cannot be obtained by experiments for several reasons. First, it is extremely difficult to apply sophisticated optical measurements techniques to a rapidly oscillating combustion engine without affecting the boundary conditions of spray development and combustion and even if this task is achieved to a satisfactory degree, there will always remain several areas of interest that are not accessible. Moreover, experiments can hardly yield three-dimensional resolved information. They are usually limited to two dimensions if light-sheets are applied or integrated information that are one-dimensional for a specific volume. Hence, the modeling of spray

www.manaraa.com

and combustion processes can help understand the in-cylinder phenomena in a cost and time effective way and benefit engine development.

Modeling of the important sub-process to predict heat release rates and exhaust emissions as a function of characteristic engine parameters is possible with proper numerical grid resolution. The spatial resolution is a concern in realistic geometries due to the size of the domain and complicated features of the geometry. Hence, dynamic mesh refinement can be used to properly resolve the sub-process of spray and combustion using a baseline coarse mesh with increased spatial resolution for better numerical accuracy.

1.2 Objectives

The goal of this study is to improve the predictive capabilities of spray breakup and combustion models. The first objective is to develop a unified spray model to be used with dynamic mesh refinement to simulate spray atomization in gasoline and diesel engines. The model will be validated by experimental data of both gasoline and diesel sprays. The second objective is to implement a chemistry model to simulate the overall combustion and emission formation process.

www.manaraa.com

CHAPTER 2. LITERATURE REVIEW

2.1 Introduction

Due to the growing importance of fuel economy and future emissions restrictions, engine manufactures are continuously forced to improve the combustion process. Despite the quantitative uncertainties of numerical simulation, modeling of fuel spray and combustion processes has significant advantages that make its utilization in current engine development a necessity. Numerical simulation can potentially provide detailed information about the complex in-cylinder process. However, accurate models are required.

To describe the sub-grid scale physics it is necessary to introduce submodels into spray computations for processes that occur on time and length scale that are too short to be resolved. Empirical correlations are introduced into these submodels to describe the unresolved physical processes. The capability and limitations of these models can be validated by comparing their results with experiments. Sub-process like atomization, drop distortion and drag, drop breakup, collision/coalescence, drop vaporization, and spray/wall interaction comes under the category which requires realistic physical models to describe them. Analytical models and controlled experiments that isolate the relevant processes have been used to generate correlations to form the basis of these submodels.

The spray and combustion process in engines consists of many sub-processes, which can be modeled by corresponding mathematical models. Engine simulation models can be divided into three groups based on the complexity, subprocess included, and computational cost. First, the thermodynamic or zero-dimensional models consider only the most relevant

www.manaraa.com

process without accounting for spatial resolution. These models are often used in applications where short computing times are more important than the details of the sub-processes.

The phenomenological spray and combustion models come under the second class of the models and use more detailed sub-models for processes such as breakup, collision and combustion. These models divide the combustion chamber into different zones based on temperatures and compositions. The spatial resolution is still coarse to completely resolve the physics taking place in the engine.

The third class of the models is multidimensional computational fluid dynamics (CFD) models that solve partial differential equations for mass, momentum, energy and species with spatial resolution. In these models detailed sub-models are used to describe the sub-processes of interest. These models can be computationally expensive than the other categories of the models mentioned above.

The study focused on direct injection engines, including both compression-ignition (diesel) and spark-ignition (gasoline) engines. Development of appropriate CFD models to describe spray, mixture formation and combustion in direct injection engines is necessary. In this chapter, a review of the spray and combustion models will be provided and a brief review of the dynamic mesh refinement will also be mentioned.

2.2 Spray Models

The engine sprays are used for mixing the liquid fuel with air. In direct-injection engines, the fuel is injected into the combustion chamber to form a combustible mixture with air. The spray and the mixture formation affect the ignition behavior, heat release, pollutant formation

www.manaraa.com

and fuel economy. The high injection pressure of fuel will also impart turbulence which complicates the spray phenomena. The interaction of the spray with the gas phase is also very complex because there is an exchange of momentum between the gas phase and liquid phase.

The spray originated from an injector can be divided into different regimes as shown in Fig. 2.1. The intact core of the liquid phase from the injector rapidly disintegrates into ligaments and further into droplets and the density of the droplets reduces as the spray moves away from the nozzle.

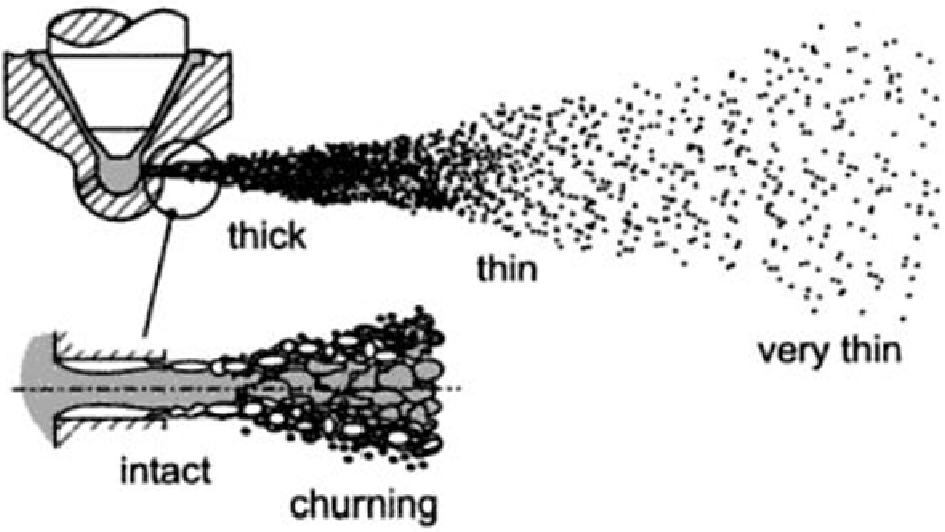

Figure 2.1 Schematic diagram of different flow regimes in a spray

The region near the nozzle has the density of the liquid phase much higher than the gas phase and is generally called a thick or dense spray region. Due to the shape of the spray and the atomization of the fuel as the spray moves further, the average spacing between the droplets increases and the volume fraction occupied by the gas phase increases. This region is called the thin spray region and the region becomes very thin and dilute as the spray moves

www.manaraa.com

further and the volume and the mass fraction of the liquid phase becomes negligible in the very thin region. The droplet-droplet interactions such as collisions and coalescence are important near the nozzle.

The liquid spray breaks up into ligaments and droplets, the first kind of breakup occuring near the vicinity of the injection nozzle orifice, i.e. in the region that has been scaled up in the bottom part of Fig. 2.1. This region is referred to as primary breakup region. The primary breakup is the breakup of the intact liquid phase into ligaments and initial droplets. The initial droplets are further distorted and subsequently broken up into smaller secondary droplets. This region is termed as secondary breakup region that takes place farther downstream of the nozzle.

The primary breakups of liquid jets at the nozzle exit are mainly caused by a combination of three mechanisms: turbulence within the liquid phase, collapsing of cavitation bubbles and aerodynamic force acting on the liquid jet. A high level of turbulence is generated within the liquid phase that has destabilizing effect on the jet once it exits the nozzle. The velocity of the jet gets accelerated due to the sharp edges at the nozzle inlet and this causes a local reduction of the static pressure inside the nozzle much less than that of the vapor pressure and causes cavitation of the bubbles. The cavitations of the bubbles are swept out of the nozzle into the combustion chamber where they implode and contribute to the disintegration of the spray. The relative velocity between the liquid jet and the gas results in aerodynamic forces that act on the liquid surface. Hence, surface disturbances develop and start to grow that lead to breakup of liquid jet as well. The injection parameters such as

www.manaraa.com

relative velocity between liquid and gas, the liquid and gas densities, and the liquid viscosity and surface tension also affect the above mechanisms and cause several breakup modes.

There are only a few detailed models available for the simulation of the primary breakup of high-pressure sprays. The experimental verification of the primary breakup models is difficult due to the complicated dense spray and the small dimensions. The mathematical description of the liquid phase inside and outside the nozzle, hence, is not possible to calculate the primary breakup directly such that appropriate models need to be used.

There are different classes of breakup models depending on the mechanisms including aerodynamics-induced, cavitation-induced and turbulence-induced breakup. The simpler the model, the less input data needed for the model and less the nozzle flow linked to primary breakup and more assumptions to be made about the upstream conditions. Detailed models will require more information about the injector flow and cause an enormous increase in computational time. Different kinds of models have different applications, depending upon the available input data and computational time.

2.1.1 Blob-Method

The “blob” is the most popular and simplest way of defining the exit conditions of the nozzle (Reitz and Diwakar, 1987). This model injects uniform spherical droplets with diameter equal to that of the nozzle. The droplet is further subject to secondary aerodynamics-induced breakup. The conservation of mass gives the initial velocity at the exit

www.manaraa.com

of the nozzle hole. The blob method is a simple and well-known method of treating the primary breakup in the Eulerian and Lagrangian CFD codes.

2.1.2 Distribution Functions

This approach uses the assumption that fuel fully atomizes at the nozzle exit and a droplet size distribution is described by mathematical functions. The measurements are difficult at the nozzle exit of the high-pressure sprays, hence, the droplet distribution should be assumed and iteratively adjusted until the far field droplets match with the measured drops. This approach is not a detailed modeling of the primary breakup, but can be an alternative for the mono-disperse injection of the blob method.

2.1.3 Turbulence-Induced Breakup

A phenomenological model of the turbulence induced atomization for diesel sprays was proposed by Huh and Gosman (1991). This model was also used to predict the primary spray cone angle. In this model the initial surface perturbations are created due to the turbulent forces within the liquid emerging from the nozzle and they grow exponentially due to the aerodynamic forces to form new droplets. The turbulent length scale determines the wavelength of the most unstable surface wave. The model is initiated with the injection of the spherical droplets of the diameter of the nozzle hole diameter. The surface waves grow due to the relative velocity between gas and drop. The drop breaks up with a characteristic atomization length scale L_A and the time scale τ_A. The characteristic atomization length scale L_A is given by

$$L_A = C_1 L_t = C_2 L_w \qquad (2.1)$$

www.manaraa.com

where L_t is the turbulent length scale, $C_1 = 2.0, C_2 = 0.5$, and L_w is the wavelength of surface perturbations determined by turbulence. The characteristic time scale τ_A is a linear combination of the turbulence time scale τ_t and the wave growth time scale τ_w,

$$\tau_A = C_3\tau_t + C_4\tau_w = \tau_{spontaneous} + \tau_{exponential} \qquad (2.2)$$

where $C_3 = 1.2$ and $C_4 = 0.5$ (Huh et al., 1998). This model also predicts the spray cone angle. The effects of cavitation are not included and the turbulence at the nozzle exit influence the primary spray break-up. This model is limited to non-cavitating flows.

2.1.4 Cavitation-Induced Breakup

A primary breakup model for diesel sprays that considers cavitation, turbulence, and aerodynamic was developed by Arcoumanis et al. (1997). This model assumes that the cavitation bubbles are transported to the blob surface by the liquid velocity inside the nozzle and either burst on the surface or collapse. The characteristic time is calculated for both conditions and the smaller one causes the breakup of the droplet. The cavitation bubbles are lumped together into a single droplet whose surface area is equal to that of the sum of the droplets and the collapse time of the cavitation bubble depends upon the radius of the bubble. The cavitation bubble which is bigger than the radius of the single bubble is used to estimate the atomization time from the Rayleigh theory (Brennen, 1995).

2.1.4 Cavitation and Turbulence-Induced Break-Up

A cavitation and turbulence-induced primary breakup model for diesel sprays were presented by Nishimura and Assanis (2000). The cavitation collapse bubble energy is taken

www.manaraa.com

into account in this model. Cylindrical ligaments with diameter equal to the blob are injected and it contains bubbles depending upon the volume fraction and size distribution at the nozzle exit. The turbulent kinetic energy and the injection velocity are also provided by this model. The energy released from the bubble collapse will increase the turbulent kinetic energy. The reduction in volume during the collapse is given by the Rayleigh theory and isotropic turbulence is assumed in this model and the turbulent velocity inside the cylinder is calculated.

2.1.5 Wave-Breakup Model

The development of this model is based upon the growth of the surface disturbances on the liquid phase (Reitz, 1987). This model is widely applied in primary and secondary breakup modeling. The cylindrical jet that penetrates from the orifice is subject to a number of infinitesimal perturbations with amplitude of η_0 and a spectrum of wavelengths λ with wave number $k = 2\pi/\lambda$. The disturbances are initially caused by the turbulence in the liquid and their amplitudes exponentially increase due to the liquid-gas interaction with a growth rate of

$$\omega = \omega_r + i\omega_i \tag{2.3}$$

$$\eta(t) = R\left(\eta_0 \exp\left[ikx + \omega t\right]\right) \tag{2.4}$$

Perturbations of different wavelengths will superimpose each other, but only the fastest growing perturbation by growth rate Ω and wavelength Λ will lead to breakup. The

www.manaraa.com

simplified expressions for the maximum growth rate Ω and corresponding wavelength Λ are obtained from Reitz (1987).

$$\frac{\Lambda}{a} = 9.02\frac{\left(1+0.45Z^{0.5}\right)\left(1+0.4T^{0.7}\right)}{\left(1+0.87We_g^{1.67}\right)^{0.6}} \tag{2.5}$$

$$\Omega\left(\frac{\rho_l a^3}{\sigma}\right)^{0.5} = \frac{0.34+0.38We_g^{1.5}}{\left(1+Z\right)\left(1+1.4T^{0.6}\right)} \tag{2.6}$$

$$Z = \frac{We_l^{0.5}}{Re_l}, T = ZWe_g^{0.5}, We_l = \frac{\rho_l U^2 a}{\sigma}, Re_l = \frac{Ua}{\upsilon_l}$$

In order to estimate the sizes of droplets formed by breakup, it is often assumed that there is a linear dependence between the droplet radius r_d and the most unstable surface disturbance Λ

2.1.6 Taylor Analogy Breakup Model

The Taylor Analogy Breakup model assumes that droplet distortion can be described as a forced, damped, harmonic oscillation. The oscillating drop that penetrates into a gaseous environment is similar to the spring-mass system. The force initiating the oscillation of the mass will correspond to the aerodynamic force distorting the droplet. The restoring force in the spring-mass system is similar to the surface tension force in the droplet. The damping force will correspond to the friction force inside the droplet due to the dynamic viscosity of the liquid. An equation for droplet distribution will be solved analytically for the time-dependent distortion amplitude. The breakup occurs if the distortion parameter exceeds unity.

www.manaraa.com

2.1.7 Kelvin-Helmholtz Breakup Model

The wave breakup theory that describes the development of Kelvin-Helmholtz instabilities was applied to the secondary breakup modeling of droplets by Reitz (1987). The breakup time was given by

$$\tau_{bu} = 3.726 B_1 \frac{r}{\Lambda \Omega} \tag{2.7}$$

The wavelength Λ and wave growth rate Ω of the most unstable surface waves are given by Eq. 2.10 and Eq. 2.11. r is the parent droplet radius equivalent to the jet radius a. The Kelvin-Helmholtz breakup model also predicts a normal velocity component of the secondary droplets after breakup. However, it should be noted that there is considerable uncertainty about the value of B_1. The value of B_1 may need to be adjusted to different initial disturbances levels of the droplets and in literature the value ranging from 1.73 up to 30. The Kelvin-Helmholtz breakup model results in a bimodal droplet size distribution with small droplets shearing off from the parent droplet and the larger droplets remaining on the original parent droplet.

2.1.8 Rayleigh-Taylor Breakup Model

Taylor (1963) investigated the stability of liquid-gas interfaces when accelerated in normal direction to the plane, and the Rayleigh-Taylor breakup model is based on these theoretical considerations. The interface is stable when acceleration and density gradient point to the same direction and Rayleigh-Taylor instabilities can develop if the fluid acceleration has an opposite direction to the density gradient. Instabilities may grow unstable

www.manaraa.com

at the trailing edge of the droplet when a liquid droplet decelerated by drags forces in a gas phase. The acceleration and deceleration of a droplet is due to drag forces

$$\left|\vec{F}\right| = \frac{3}{8} C_D \frac{\rho_g v_{rel}^2}{\rho_l r} \tag{2.8}$$

where v_{rel} the relative velocity between droplet and gas, and r is the droplet radius. The frequency and wavelength of the fastest growing waves are

$$\Omega = \sqrt{\frac{2\left|\vec{F}\right|}{3}} \times \left[\frac{\left|\vec{F}\right|\left(\rho_l - \rho_g\right)}{3\sigma}\right]^{1/4} \tag{2.9}$$

$$\Lambda = 2\pi \sqrt{\frac{3\sigma}{\left|\vec{F}\right|\left(\rho_l - \rho_g\right)}} \tag{2.10}$$

The acceleration causes the rapid growth of Rayleigh-Taylor instabilities and the surface tension counteracts the breakup mechanism. The breakup time found as the reciprocal of the frequency of the fastest growing wave as

$$t_{bu} = \Omega^{-1} \tag{2.11}$$

The Rayleigh-Taylor breakup model is usually applied to describe the secondary droplet breakup and Kelvin-Helmholtz model describe stripping breakup. The Kelvin-Helmholtz and Rayleigh-Taylor are implemented in a competing manner. The droplets breakup mechanism that predicts a shorter breakup mechanism are used as breakup mechanism.

www.manaraa.com

2.3 Combustion Models

The diesel engine in-cylinder combustion process is a complicated process and has to be studied using computational models with proper attention to spray development, vaporization, mixture formation and combustion process. The development and application of engine CFD models have become increasingly important and effective in analyzing the complex diesel combustion process involved. Diesel combustion models are mainly classified into two groups, thermodynamic and multidimensional models. The thermodynamic models are concerned with energy conversion and are mainly used to calculate heat release rate based on a given pressure history. The multidimensional models intend to describe the real engine process by considering spatial variation of flow field, temperature, composition, pressure and turbulence within the combustion chamber and are more informative about combustion phenomena. The physics and chemistry involved in combustion process of diesel engine is one of the most challenging in modeling diesel combustion. In diesel engines, the process shortly after ignition is believed to be premixed burning and the subsequent process is thought to be mixing-controlled combustion process and is characterized as diffusion burning. Hence, the modeling of combustion needs take account of both the premixed and diffusion burn.

The combustion of simple hydrocarbons such as methane is subject to very complex reaction mechanisms and involves numerous species and reactions. For example, Frenklach et al. (1992) has proposed a methane combustion scheme consisting of 149 reactions and 33 chemical species. The long hydrocarbons used in diesel engines have even more complicated reaction mechanisms and are computationally costly to solve. It is important to create

www.manaraa.com

reduced mechanisms with smaller number of species and reactions that are able to describe the combustion characteristics to a reasonable level of details. The global single-step mechanism gives a rough estimate of the heat release rate, but does not give details about the intermediate species formation and oxidation. Multi-step mechanisms can give details about these intermediate species and rate-controlling reaction steps.

Different flame regimes can be identified depending on the mixture state and the interactions between chemistry and turbulence. The flames can be mainly distinguished into two types, premixed and diffusion, depending on the mixing of fuel and oxidizer homogenously prior to combustion or mixing during the combustion.

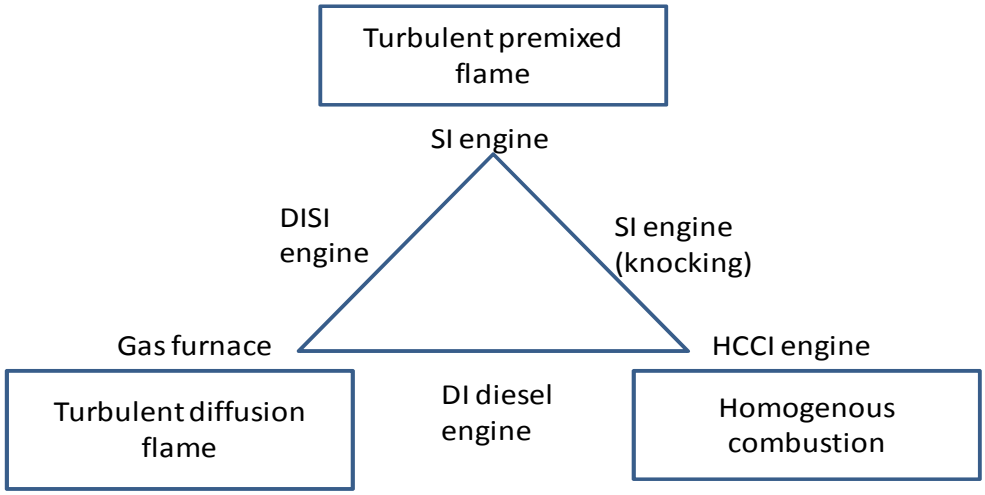

Figure 2.2 Flame types in combustion engines (Stiesch, 2004)

In an engine combustion chamber, the gas flow turbulent and Fig. 2.4 shows relative applications in which the respective combustion types can be observed. The following is a review of ignition and combustion models which are used to simulate diesel combustion.

www.manaraa.com

2.3.1 Single-step mechanism

A single-step reaction expressed by an Arrhenius equation is assumed in this model and the production rate of the radical species becomes the reciprocal value of the formal ignition delay. The ignition delay is expressed as

$$\tau_{id} = C_{id} \frac{1}{j \times P^2} \exp\left(E_{id}/T\right) \tag{2.12}$$

where E_{id} is the activation temperature, T and P are temperature and pressure and j is the equivalence ratio. The increase of the ignition delay for an increasing temperature due to the degenerated chain branching reactions cannot be predicted with this single step method (Otto, et al., 1998).

2.3.2 Shell Model

The Auto ignition Shell model originally developed by Halstead et al. (1977) for spark ignition engines was adjusted and applied to model diesel ignition (Kong, et al., 1995). This model is the most widely used ignition model in engine modeling. It consists of eight reaction steps between five species to simulate the ignition behavior of hydrocarbon-air mixtures. The model considers multistage ignition and cool flame phenomena using the following reactions.

$$RH + O_2 \xrightarrow{k_q} 2R^* \tag{2.13}$$

$$R^* \xrightarrow{k_p} R^* + P + Heat \tag{2.14}$$

$$R^* \xrightarrow{f_1 k_p} R^* + B \tag{2.15}$$

www.manaraa.com

$$R^* \xrightarrow{f_4 k_p} R^* + Q \tag{2.16}$$

$$R^* + Q \xrightarrow{f_2 k_p} R^* + B \tag{2.17}$$

$$B \xrightarrow{k_b} 2R^* \tag{2.18}$$

$$R^* \xrightarrow{f_3 k_p} \text{termination} \tag{2.19}$$

$$2R^* \xrightarrow{k_t} \text{termination} \tag{2.20}$$

RH indicates fuel, R^* is the generalized radical, B is the branching agent, and P denotes oxidized products. The species concentration can be solved numerically by integrating differential equations. The rate of change of the intermediate species, oxygen and fuel are

$$\frac{d[R^*]}{dt} = 2k_q[RH][O_2] + 2k_b[B] - f_3 k_p[R^*] - k_t[R^*]^2 \tag{2.21}$$

$$\frac{d[B]}{dt} = f_1 k_p[R^*] + f_2 k_p[R^*][Q] - k_b[B] \tag{2.22}$$

$$\frac{d[Q]}{dt} = f_4 k_p[R^*] - f_2 k_p[R^*][Q] \tag{2.23}$$

$$\frac{d[O_2]}{dt} = -pk_p[R^*] \tag{2.24}$$

$$\frac{d[RH]}{dt} = \frac{[O_2] - [O_2]_{(t=0)}}{p \times m} + [RH]_{t=0} \tag{2.25}$$

www.manaraa.com

where m is related to the number of hydrogen atoms in the fuel C_nH_{2m} and p is calculated from

$$p = \frac{n(2-\gamma)+m}{2m}. \tag{2.26}$$

The Shell model can predict the negative temperature coefficient observed in auto ignition phenomena under engine-like conditions.

2.3.3 The Characteristic Time Scale Model

The laminar and turbulent characteristic time scale model has been used to model combustion in diesel engines (Kong et al. 1995). The change in species density in terms of characteristic time scale and actual and equilibrium mixture compositions are

$$\frac{d\rho_i}{dt} = -\frac{\rho_i - \rho_i^{eq}}{\tau_c} = -\frac{\rho_i - \rho_i^{eq}}{\tau_l + f\tau_i}. \tag{2.27}$$

The delay factor f and r as a function of local composition is given below

$$f = \left(1 - e^{-r}\right)/0.632 \tag{2.28}$$

$$r = \frac{Y_{CO_2} + Y_{H_2O} + Y_{CO} + Y_{H_2}}{1 - Y_{N_2}} \tag{2.29}$$

The parameter r value varies from zero to unity for unburned and completely burned mixture. The delay factor f also varies from zero and unity. The turbulence driven microscale mixing

www.manaraa.com

becomes more important compared to the chemistry effects as the combustion propagates. The laminar and turbulent time scale for diesel fuel is given as

$$\tau_l = A^{-1}\left[C_{14}H_{30}\right]^{0.75}\left[O_2\right]^{-1.5}\exp\left(E_A/RT\right) \tag{2.30}$$

$$\tau_t = 0.142\times k/\varepsilon. \tag{2.31}$$

The pre-exponential constant and the activation energy are $A = 7.68\times10^{8}$ and $E_A = 77.3\,KJ/mol$, respectively. The characteristic time scale combustion model has been applied in many studies of diesel engine combustion. The time scale combustion model is better suited to describe non-premixed combustion. The turbulent mixing of reactants is primarily governed by the dissipation of the large scale eddies in diesel combustion.

2.3.4 Flamelet Models

In the flamelet approach, substantial fraction of chemical reactions is assumed to take place in the thin layers and is locally treated as laminar reaction sheets (Peters, N., 1984 and Peters, N., 1986). This is justified as the chemical time scales are typically short compared to diffusion and convection time scales. The turbulent flame brush is viewed as an average of numerous laminar flamelets subject to the statistical probability distribution similar to the turbulent fluctuations of the flow field. In these thin laminar flamelets, combustion can be treated as a process that depends only on the mixing between fuel and oxidizer. The mixture fraction Z is the ratio of the fuel mass flow rate to the total mass flow rate.

$$Z = \frac{\dot{m}_{fuel}}{\dot{m}_{fuel} + \dot{m}_{oxidizer}} \tag{2.32}$$

www.manaraa.com

The mixture fraction is not affected by combustion but only by mixing. In this approach, the change in species density due to chemical reactions is solved one dimensionally as a function of mixture fraction only. The results of these calculations can be stored in lookup tables and can be made readily available when the actual CFD calculation is performed. The chemistry has to be solved only once for a set of flamelet boundary condition, hence complicated chemical mechanisms can be used without the penalty of computational cost.

The effects of turbulent fluctuations on combustion are accounted for by weighing the one-dimensional flamelet results with the probability that the flamelet is found in a computational cell. The integration of these weighted flamelet solution is executed over all possible flamelets to obtain the overall solution for the new composition within each CFD grid cell, where $\tilde{Y}_i$ indicates the Favre-averaged mass fraction of species i in a grid cell in the following given equation.

$$\tilde{Y}_i = \int_0^1 P(Z) \times Y_i(Z).dZ \qquad (2.33)$$

Flamelet models can provide a platform for implementing the detailed chemical mechanisms with less computational resources than other models for non-premixed combustion.

2.4 Dynamic Mesh Refinement

The engine sprays in internal combustion engines are widely modeled by the Lagrangian and Eulerian approach, and the gas phase in the modeling are described using the Eulerian approach. The numerical solution of the Navier-Stokes equations may become more accurate

www.manaraa.com

if the grid is refined, due to the way the differential equations are discretized and the differential coefficients are approximated. To achieve accurate results, the grid resolution needs to be fine enough to resolve the physical scales of the problem. The liquid phase is modeled by Lagrangian approach and the grid resolution also effects the Lagrangian liquid phase description. If the Eulerian field is not properly computed in the vicinity of the liquid phase, diffusion may be over-estimated and can lead to inaccurate results. The reduction of the grid size for the Eulerian phase to very small may cause a limitation on the Lagrangian liquid phase description, because it is based on the assumption of a large void fraction within a cell. In contrast, the coarse grid size for the Eulerian phase can predict an incorrect gas-droplet momentum exchange. The dynamic mesh refinement adapted to spray is an appropriate option to partially alleviate the grid resolution problem. The adaptive methods are generally characterized as r-refinement, h-refinement and p-refinement.

2.4.1 r-refinement

In r-refinement a fixed-topology mesh is concentrated in regions where enrichment indicators are high. This enrichment criterion is a weighting function, which is large where a high grid resolution is required and small elsewhere. This function would lead to low node density where solution variation is small and increased node density where the variation is large. The standard weighting function could be a primitive variable, a derived quantity or any identifiable characteristic of the solution that needs increased resolution. Once the weighting function is found, it should be considered to be a mass associated with each mesh node. This information can be used to reallocate the mesh nodes in a direction toward the

www.manaraa.com

center of mass for a local collection of cells. Then the mesh node reallocation is done and the solution redistribution occurs in the computational space.

The main advantage of this refinement is that dynamic and automatic adaptation for both steady and unsteady solution can be found with constant computational resources. It can also adapt to many features simultaneously and tend to align mesh with strong features of the solutions with efficient use of mesh nodes. The disadvantages include that surface geometry is not preserved as nodes translate on the surface and errors may increase when cell surface movement is more than one local cell dimension.

2.4.2 p-refinement

In p-refinement the order of numerical approximation is varied locally. In this refinement the initial mesh is kept the same and there is a selective increase in the order of the polynomial. One of the most important advantages of p-refinement is the ability to produce the exponential decay of the dicretization errors for sufficiently smooth solutions. The effectiveness of p-refinement also depends on the number of elements and its uniformity, the form of geometric singularities and the discontinuities in boundary conditions. These factors degrade convergence because they propagate into the high-order components of the solution that would otherwise be exponentially small. To circumvent this problem with p-refinement, it often selects a fixed good mesh, i.e., one that is sufficiently refined near potential singularities. Thus, these troubling factors can be isolated and the error can be decreased exponentially. The fast convergence of p-refinement is achieved at the expense of significantly increased computational cost.

www.manaraa.com

2.4.3 h-refinement

The h-refinement method is to add more nodes in regions where a higher accuracy is desired. In this refinement either mesh is refined or coarsened by adding or removing cells. With h-refinement it is possible to reduce the error in the domain by selectively increasing the number of nodes. The h-refinement is both used in Cartesian mesh and unstructured mesh.

One can decrease error in the solution on a computational mesh by increasing the number of nodes in the mesh. It has been shown that the error decreases when the number of nodes is increased in a regular mesh. However, in the case of an irregular mesh, the addition of nodes must be selective, since the distribution is not less important than the number of nodes. It is interesting to note that not only number, but location of nodes influences finite difference operator quality and that is recommended to use good quality clouds of nodes. At the same time it is necessary to realize increasing the number of nodes may decrease the solution error, but it does not change precision of finite difference operators. In order to avoid ill-conditioning clouds, a limit for the distance between nodes is used as a second parameter minimum distance such that if the distance between the new node and any node of the domain is smaller than this minimum distance, the new node should not be added. This minimum distance is an important parameter involved for the control of the h-refinement procedure and it is given as the maximum distance between all the nodes of the mesh, multiplied by a positive parameter.

www.manaraa.com

h-refinement does not have all the disadvantages mentioned in the other types of refinement and is flexible to apply to a multi-dimensional CFD code. It is also less difficult to implement the h-refinement and use it with sub-models in a multi-dimensional CFD code.

www.manaraa.com

CHAPTER 3. UNIFIED SPRAY MODEL

3.1 Introduction

One of the key issues to simulating the direct-injection gasoline and diesel engines is the proper prediction of the fuel spray at the nozzle exit, primary breakup, secondary atomization, droplet collision, and the interaction of spray particles and gas. Advanced physical models and accurate numerical schemes are required. It is known that the prediction of the fuel spray is sensitive to the grid resolution. An adequate grid resolution is required to obtain accurate results, especially in the dense spray region where the velocity and species gradients are strong (Abraham, 1997; Berad et al., 2000; Hieber, 2001).

Engine sprays are widely modeled by the Lagrangian-drop and Eulerian-fluid technique. The Lagrangian-Eulerian technique was based on the particle-fluid numerical model by Dukowicz (1980), also known as the stochastic parcel method. In this method, the spray was represented by collective computational parcels. Each computational parcel consisted of a number of droplets that were often assumed to have identical properties such as velocity, density, radius, temperature and position. On the other hand, there were other approaches based on an Eulerian-Eulerian formulation for spray (Wan and Peters, 1997; Von Berg et al., 2003; Blokkeel et al., 2004; Beck and Watkins, 2004). Blokkeel et al. (2004) formulated an Eulerian model to improve the primary breakup of the atomizing jet. This model used an Eulerian formulation for the spray close to the injector and a Lagrangian formulation for the remaining dilute spray. This model had numerous advantages but the implementation of other spray submodels based on this framework was relatively

www.manaraa.com

cumbersome. The Eulerian-Eulerian formulation to describe the complicated diesel spray was also discussed by Baumgarten (2006).

In the Lagrangian-Eulerian approach, the Eulerian mesh for the gas phase simulation needs to be adequate in order to avoid the mesh dependence. If the Eulerian field is not properly computed in the vicinity of the liquid phase, diffusion may be over-estimated and lead to inaccurate results. The reduction of the grid size for the Eulerian phase to very small may cause a limitation on the Lagrangian liquid phase description. The Lagrangian liquid phase description is based on the assumption of a large void fraction within a cell. The coarse grid size for the Eulerian phase can predict an incorrect gas-droplet momentum exchange. The momentum gain from the droplets is transferred uniformly to the cell, hence, fast diffusion of momentum will occur using a coarse grid and the predicted spray penetration will be reduced. On the other hand, a cell volume smaller than the actual area of influence of the droplet will cause the gas velocity to exceed the actual velocity, which in turn results in a longer spray penetration. The grid resolution can also affect the collision algorithm used in the model and further influence the simulation results (Schmidt and Rutland, 2000; Subramaniam, 1988; Beard, 2000; Hieber, 2001).

The dynamic mesh refinement adapted to spray is an appropriate option to partially alleviate the grid resolution problem. A fine grid resolution is needed primarily in the spray region and the dynamic mesh refinement adapted to spray can increase the grid resolution in the spray region. Various adaptive mesh refinement algorithms were developed for numerous purposes (Bell et al., 1994; Biswas and Strawn, 1998; Jasak and Gosman, 2000). Nomura et al. (2001) used adaptive mesh refinement for direct-injection gasoline engine simulation. The

www.manaraa.com

refinement was focused on a fixed region without the capability to refine the mesh dynamically. Lippert et al. (2005) used least-squares fitting for gas-to-liquid coupling and kernel smoothing for liquid-to-gas coupling based on dynamic mesh refinement to improve the efficiency of spray modeling. Local mesh refinement using h-refinement was also developed to improve the accuracy and computational efficiency of spray simulation (Xue et al. 2008; Xue and Kong, 2009).

On the other hand, the accurate prediction of the spray dynamics requires the use of advanced spray submodels. The internal flow in the nozzle, especially for diesel injectors, may experience separation and cavitation that can enhance the turbulence level of the spray. The nozzle geometry and the flow characteristics inside the nozzle strongly affect the initial liquid jet conditions. Thus, a model to predict the nozzle flow is needed to provide the initial fuel spray conditions. Studies were performed to model the injection process by considering the detailed nozzle geometry and needle lift (Arcoumanis et al., 1997; Hountalas and Kouremenos, 1998). A nozzle model was also available to predict possible flow regimes for different injector geometries and injection conditions (Sarre et al., 1999).

The fuel spray was usually modeled for primary breakup and secondary breakup separately. The initial droplets and ligaments formed from the liquid jet were modeled using the primary breakup model. Various models were available to simulate the primary breakup induced by aerodynamic, cavitation, or turbulence forces. The model by Reitz and Diwakar (1987) was a blob method that was based on the assumption that jet breakup and drop breakup near the nozzle were indistinguishable processes. Huh and Gosman (1991) and Arcoumanis et al. (1997) assumed that droplets were formed due to the surface perturbations

www.manaraa.com

resulting from aerodynamic forces. Nishimura and Assanis (2000) presented a primary breakup model that considered the cavitation bubble collapse energy. Yi and Reitz (2003) proposed a 1-D model based on the surface wave growth to predict the primary breakup.

The breakup of droplets and ligaments formed from the primary breakup were modeled using the secondary breakup model. O'Rourke and Amsden (1987) proposed a model based on the analogy between a forced oscillating spring-mass system and the drop deformation that resulted in breakup. Patterson and Reitz (1998) developed a hybrid Kelvin-Helmholtz / Rayleigh-Taylor (KH/RT) model for diesel spray modeling. The KH model was based on the surface wave instability that induced the shearing-off of droplets, and the RT model was based on the instability resulting from the deceleration of the drops due to the relative velocity between the gas and liquid phases. Beale and Reitz (1999) also applied this model for gasoline spray simulation.

This study implemented various spray submodels, including nozzle flow, primary breakup, and secondary breakup models, into an engine simulation code that was capable of performing dynamic mesh refinement. Note that traditionally gasoline sprays and diesel sprays were simulated using different models (Stiesch, 2004; Baumgarten, 2006). Even though the same model was used, different model constants were often required (Beale and Reitz, 1999; Kong et al., 1999). The present study used the same set of models and constants to simulate both gasoline and diesel sprays under different conditions. Additionally, the previously developed dynamic mesh refinement scheme was not validated using experimental spray data (Xue and Kong, 2009). In this study, the mesh refinement algorithm

www.manaraa.com

was further improved and the resulting numerical model was validated using experimental spray data and was also applied to simulate sprays in realistic engine geometries.

3.2 Model Formulation

3.2.1 Base CFD Code

The CFD code used in this study was KIVA-4 (Torres and Trujillo, 2006; Torres, 2007). KIVA-4 solves the three-dimensional compressible Navier-Stokes equations and is capable of using unstructured meshes. KIVA-4 uses the Lagrangian-Eulerian methodology to simulate engine sprays. The original KIVA-4 (Torres and Trujillo, 2006) used a "staggered" approach, in which the velocity was assigned at the node while the remaining cell properties (density, temperature and pressure) are assigned at the cell center. Note that the version used in this study was based on the "collocated" approach that assigned all cell properties at the cell center, including the velocity (Torres, 2007). The collocated version of KIVA-4 was used for the development of dynamic mesh refinement to ease the use of an overly fine mesh (Xue and Kong, 2009). The collocation of velocity at the cell center had the advantage of prescribing velocity boundary conditions on the cell faces rather than at the nodes. The Lagrangian particles were coupled with cell-centered grid velocity in the spray term of the momentum equation.

The representation of pressure and velocity at the cell center can cause unphysical pressure oscillations (Tsui and Pan, 2006). The Rhie-Chow technique was used to mitigate these oscillations when computing face velocities. The conservation equations were solved in three stages. In Stage 1, the spray and chemical source terms were updated, In Stage 2,

www.manaraa.com

diffusion calculations are performed. The equations were solved using a SIMPLE algorithm implicitly and a conjugate residual method was used to solve the equations. The final stage was the rezoning (Eulerian) phase in which the flow field was frozen but cell vertices were moved to new positions and the flow field was rezoned on the new mesh. Further details about KIVA-4 can be found in Torres and Trujillo (2006).

3.2.2 Dynamic Mesh Refinement Algorithm

The schematic of mesh refinement is shown in Figure 3.1. The basic conservation equations for the development of dynamic mesh refinement can be found in Xue and Kong (2009). The implementation of dynamic mesh refinement in the collocated KIVA-4 required modifications in numerical schemes for the calculation of diffusive and convective fluxes and dynamic timestep adjustment. These changes are mainly due to the coarse-fine interface between the child and parent cells**.** This study differs from the previous work (Xue and Kong, 2009) in improved algorithms for mesh refinement and enhanced numerical schemes to obtain the second-order accuracy for flux calculation, as discussed below.

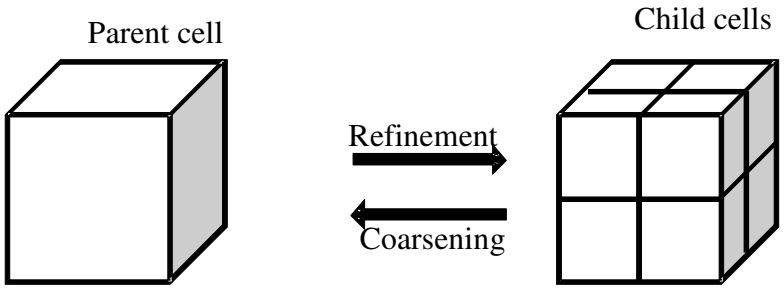

Figure 3.1 Schematic of the refinement and coarsening of cells.

www.manaraa.com

The diffusion flux terms with the form $\int_s \nabla Q * dA$ in the conservation equations are the area integrals over surfaces of cells, which can be calculated as the sum over the cell faces using a quadrature rule.

$$\int_s \nabla Q * d\boldsymbol{A} \approx \sum_f (\nabla Q)_f * \boldsymbol{A}_f \tag{3.1}$$

$$(\nabla Q)_f * \boldsymbol{A}_f = a_c(Q_c - Q_{cn}) + a_{12}(Q_1 - Q_2) + a_{34}(Q_3 - Q_4) \tag{3.2}$$

The subscript f represents the cell face, Q_c, Q_{cn} are the cell-centered values of the cells connected to face f. Q_1, Q_2, Q_3, Q_4 are the edge-centered values of the four edges bounding face f, as shown in Figure 3.2. These quantities are obtained by averaging the cell-centered values of the cells connected to the edge. The geometric coefficients a_c, a_{12} and a_{34} in Eq. (3.2) are computed by solving the equations

$$a_c(x_c - x_{cn}) + a_{12}(x_1 - x_2) + a_{34}(x_3 - x_4) = A_f \tag{3.3}$$

www.manaraa.com

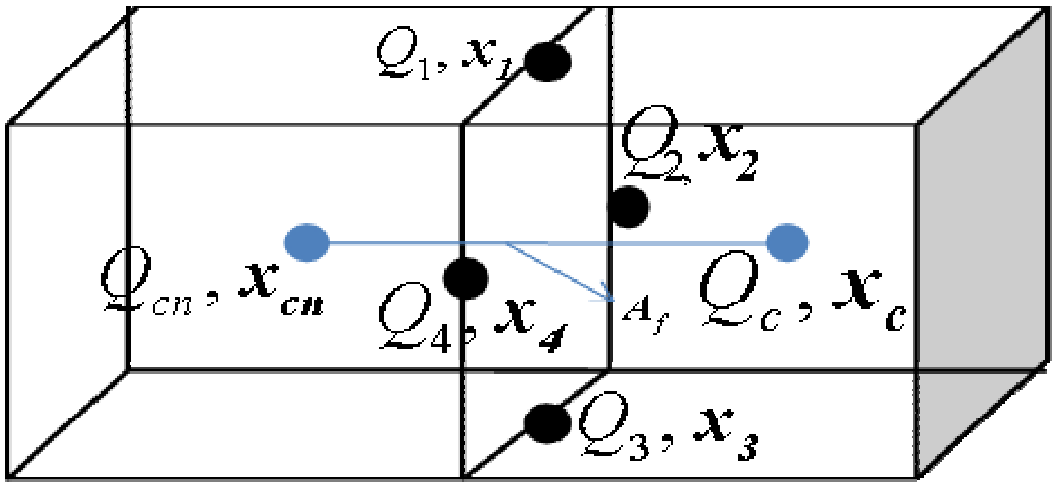

Figure 3.2 Geometric arrangement of points to define the gradient of cell-centered quantity Q on cell face f .

where x_c, x_{cn} are the centers of the cells connected to face f and x_1, x_2, x_3, x_4 are the centers of the four edges bounding face f . A_f is the face area vector of face f . If face f is an interface between four child cells and one parent cell, the fluxes at the interface will be computed as

$$(\nabla Q * A)_{pf} \approx -\sum_{c} (\nabla Q * A)_{cf} \tag{3.4}$$

where pf is the parent face, c is the child cell faces, and cf is the child face, as shown in

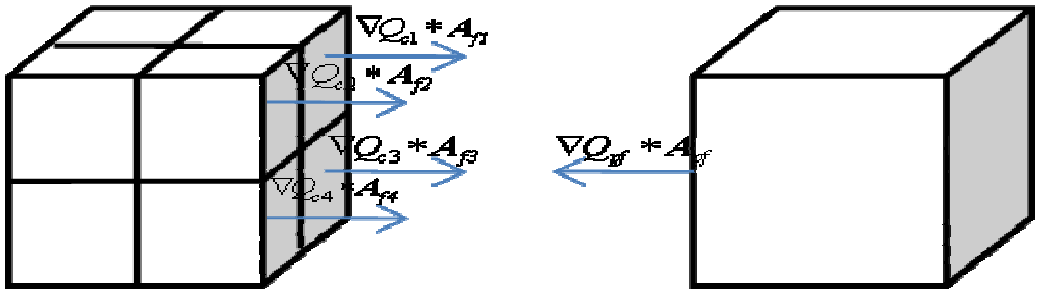

Figure 3.3 Gradient calculation at the interface f of the child cells and parent cell.

www.manaraa.com

The viscous stress tensor $\int_s \sigma * dA$ in the momentum equations is approximated in the same way as in Eq. (3.1).

$$\int_s \sigma * dA \approx \sum_f \sigma_f * \boldsymbol{A}_f \tag{3.5}$$

If face f is an interface between the parent cell and four child cells, the term in the left-hand side of Eq. (3.5) is approximated as

$$(\sigma * \boldsymbol{A})_{pf} \approx -\sum_c (\sigma * \boldsymbol{A})_{cf}. \tag{3.6}$$

The term $(u * \boldsymbol{A})_f^L$ is used to calculate the Lagrangian cell volume V^L that appears in the pressure iteration. This term is also approximated in the same way as above for the coarse-fine interface.

$$(u * \boldsymbol{A})_{pf}^L \approx -\sum_c (u * \boldsymbol{A})_{cf}^L \tag{3.7}$$

When the mesh is moved with the fluid in the Lagrangian phase, the mesh is rezoned to the new location, which leads to the convective transport of the flow fields due to the relative movement of the mesh. The total computational timestep is explicitly sub-cycled. The number of the sub-cycles is the ratio of $\Delta t/\Delta t_c$, where Δt is the main computational timestep and Δt_c is the convective timestep that satisfies the Courant condition.

At each sub-cycle the face volume change δV_f associated with cell face f is calculated by considering the total face volume change from the Lagrangian position to the

www.manaraa.com

final position after rezoning. The convective fluxes in the conservation equations are explicitly sub-cycled and the flux through a normal face into a cell is calculated as

$$(\rho QV)_c^s = (\rho QV)_c^{s-1} + (\rho Q)_f^{s-1} * \delta V_f \tag{3.8}$$

where ρ is the density, V is the volume, c is the cell considered, s is the current sub-cycle, $s-1$ represents the previous sub-cycle, and Q represents the cell-centered quantity. $(\rho Q)_f$ is determined by using a quasi-second-order upwind (QSOU) scheme at each sub-cycle. If the face is a coarse-fine interface, Eq. (3.8) will change to

$$(\rho QV)_p^s = (\rho QV)_p^{s-1} - \sum_c (\rho Q)_{fc}^{s-1} * \delta V_{fc} \tag{3.9}$$

where p represents the parent cell and c is the number of child cell at the coarse-fine interface face.

The criterion for adaptive refinement and coarsening was based on the sum of the mass of liquid and fuel vapor in a cell. The threshold was 1.0e-6 g above which a cell would be refined. This value was determined by a sensitivity analysis and was appropriate for engine spray simulation (Xue and Kong, 2009).

3.2.3 Nozzle Flow Model

A nozzle flow model provides initial spray conditions for the subsequent breakup simulation. In direct-injection gasoline and diesel engines, the injector nozzle geometry affects the fuel atomization and also influences engine combustion and emissions. The nozzle flow model (Sarre, et al., 1999) that can specify the initial fuel jet conditions was

www.manaraa.com

implemented in this study. The conditions inside the nozzle can be estimated from the nozzle geometry (diameter d, r/d and l/d ratio), injection pressure, and ambient pressure (p_2). The model output includes discharge coefficient (C_d), effective velocity (U_{eff}), average turbulent kinetic energy, spray angle, and initial drop size. The nozzle upstream pressure (p_1) can be initially estimated and will be modified depending on the type of flow inside the nozzle.

The pressure at vena contracta is then computed and compared with the saturated vapor pressure (p_{vapor}) to decide whether cavitation occurs in the nozzle. The values of p_1, C_d and U_{eff} can be determined by the following relations.

$$p_1 = p_{vapor} + \frac{\rho}{2} * U_{vena}^2 \tag{3.10}$$

$$C_d = C_c * \sqrt{\frac{p_1 - p_{vapor}}{p_1 - p_2}} \tag{3.11}$$

$$U_{eff} = U_{vena} - \frac{p_2 - p_{vapor}}{\rho_l * U_{mean}} \tag{3.12}$$

The nozzle contraction coefficient (C_c) and velocity at the vena contracta (U_{vena}) are determined by the nozzle geometry. The mean flow velocity (U_{mean}) is calculated based on the flow rate and nominal nozzle area (Sarre, et al., 1999).

www.manaraa.com

3.2.4 Primary Breakup Model

The breakup of the liquid jet at the nozzle exit was modeled using a primary breakup model (Yi and Reitz, 2003) by which the secondary droplets were created. The model tracks the growth of the disturbance on the jet surface leading to the generation of droplets. The surface structure obtained from the model is decomposed into a combination of waves using a fast Fourier transform. Initially, a disturbance, which is a combination of waves due to the nozzle flow, is applied to the undistributed jet leaving the nozzle exit. The initial disturbance is represented as

$$R(0,x) = R_0 + \frac{1}{n}\sum_{i=1}^{n}\eta_i \sin\left(\omega_i x + \varphi_i\right) \tag{3.13}$$

$$\eta_i = \eta_0 * f\left(\lambda_i\right) \tag{3.14}$$

where R is the initial jet radius at axial position x. R_0 is the undisturbed jet radius, φ_i is the phase of the i_{th} wave, n is the number of waves. η_i is the initial amplitude, η_0 is the amplitude of the most probable wave with a wavelength λ_0. $f\left(\lambda_i\right)$ is the value of the normalized Gaussian distribution for the i_{th} wave, where $f\left(\lambda_0\right)=1$. The tracking of the disturbance growth is accomplished using a 1-D model approach,

$$\frac{\partial R^2}{\partial t} = -\frac{\partial R^2 u}{\partial x} \tag{3.15}$$

$$\frac{\partial R^2 u}{\partial t} + \frac{\partial R^2 u^2}{\partial x} = -\frac{R^2}{\rho_l}\left(\frac{\partial p_l}{\partial x} + \frac{\partial p_g}{\partial x}\right) + 2\nu_l \frac{\partial}{\partial x}\left(R^2 \frac{\partial u}{\partial x}\right) \tag{3.16}$$

www.manaraa.com

where t is time, x is the axial coordinate with its positive direction pointing in the flow direction of the jet. $R = R(t, x)$ and $u = u(t, x)$ are the velocity and radius of the liquid jet, respectively, as a function of time and axial position, and ρ_l and ν_l are the density and viscosity of the liquid, respectively.

The jet surface structure obtained from the model is divided into a breakup zone and a liquid core. Drops are stripped from the breakup zone after a breakup time is achieved and their number depends on the mass of liquid in the breakup zone. The jet surface area increase due to the unstable wave growth is compared with the surface area of the drops formed from the breakup zone to determine the time of breakup. The initial breakup time and the drop diameter are calculated by choosing $\lambda_0 = 20\mu m$, $\eta_0 = 0.01\lambda_0$. Further details about the model can be found in Yi and Reitz (2003).

3.2.5 Secondary Breakup Model

The further breakup of already existing droplets into smaller droplets takes place subsequently and was simulated by a secondary breakup model. The breakup of droplets takes place due to the aerodynamic forces that are induced by the relative velocity between the droplet and the surrounding gas. In the model, unstable waves are allowed to grow on the droplet surface due to these aerodynamic forces leading to further atomization. The model used for the secondary breakup was the hybrid KH/RT model (Patterson and Reitz, 1998; Beale and Reitz, 1999). The KH model is based on a first-order linear analysis of the KH instabilities growing on the surface of a cylindrical jet (Reitz, 1987). This model was

www.manaraa.com

previously applied to drop atomization modeling by monitoring the surface wave growth rate Ω and wavelength Λ (Reitz, 1987). Child droplets are formed when breakup criteria are met.

The radius of the child drop $(r^{'})$ is proportional to the wavelength Λ of the most unstable surface wave,

$$r^{'} = B_0 * \Lambda \tag{3.17}$$

where B_0=0.61 is a constant. The mass of the parent drop is reduced based on the mass conservation. The reduction of the radius of the parent drop depends on the initial size of the parent drop (r) and the breakup time τ.

$$\frac{dr}{dt} = -\frac{r - r^{'}}{\tau} \tag{3.18}$$

$$\tau = 3.788 * B_1 \frac{r}{\Lambda * \Omega} \tag{3.19}$$

The value of B_1 is equal to 40 in this study.

The RT model is based on the theory of Taylor (1963) on wave stability. The interface between the gas and liquid is unstable when the acceleration is directed into the gas and the unstable disturbances can grow with acceleration. Due to the deceleration of the drop due to the drag forces, unstable waves can grow on the backside of the drop and the disintegration of the drop will take place when a critical limit is achieved. The acceleration of the interface of the gas and the drop due to the drag force can be found as

www.manaraa.com

$$a = \frac{3}{8} C_D \frac{\rho_g u_{rel}^2}{\rho_l r} \tag{3.20}$$

Where C_D is the drag coefficient of the drop, u_{rel} is the relative velocity between the gas and liquid drop, ρ_g and ρ_l are the gas density and liquid drop density, respectively. The linear stability analysis is used to find the growth rate Ω and the corresponding wavelength Λ of the fastest growing wave (Patterson and Reitz, 1998). The new drop radius and the breakup timescale can be determined from

$$r' = \frac{C_3 * \Lambda}{2} \tag{3.21}$$

$$\tau = \frac{1}{\Omega} \tag{3.22}$$

where r' the radius of the new drop and τ is the breakup time. The model tracks the time of the individual drop since last breakup. When breakup time is reached, new drops are formed with radius r' and the breakup time is reset to zero.

In the secondary breakup region, both the KH and RT models are allowed to grow the unstable waves simultaneously. The disintegration of a drop will occur when one of the KH or RT models predicts breakup to occur.

3.3 Results and Discussions

The present model with dynamic mesh refinement was applied to simulate both gasoline and diesel sprays. The computational domain was a constant-volume cylindrical chamber with 100 mm in diameter and 100 mm in length, as shown in Figure 3.4. The average mesh

www.manaraa.com

size was 5.0 mm before the refinement of the cells. Note that the base mesh was relatively coarse and the mesh would be refined in the spray region by the present mesh refinement algorithm. The experimental data used for gasoline spray validation included spray images and penetration data of a 10-hole gasoline injector that was used in direct-injection gasoline engines. The present model was also validated using the high-pressure diesel spray data obtained from high-pressure, high-temperature conditions in a constant-volume chamber Siebers (1998). The model was also used to simulate the gasoline sprays in realistic engine geometry.

Liquid phase fuel penetration is one of the important issues with respect to optimizing in-cylinder processes in diesel engines, especially for the direct-injection engines. Penetration of the liquid phase fuel is needed to promote fuel-air mixing, but can also lead to greater emissions if liquid fuel impinges and collects on the piston bowl. Hence, developing a better understanding of the parameters and processes that control the extent of the liquid-phase fuel in a diesel spray is important, both to the engine designer and to those developing multi-dimensional computational models for use as engine design and optimization tools.

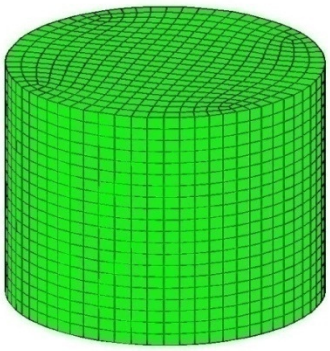

Figure 3.4 Computational mesh of the cylindrical chamber for model validation.

www.manaraa.com

3.3.1 Gasoline Spray Modeling

The test conditions for gasoline spray experiments are listed in Table 3.1. Figure 3.5 showed the computational mesh and drop and vapor distributions on a cut-plane. It can be seen that the spray penetrations varied with different mesh resolutions. Extensive studies on the present mesh refinement scheme have been documented (Xue and Kong, 2009). Therefore, this study will only present results using mesh refinement with the present spray models.

Table 1 Conditions for the gasoline sprays.

Fuel	Gasoline
Ambient gas pressure	1 bar to 5 bar
Ambient gas density	1.15 to 5.8 kg/m^3
Ambient gas temperature	300 K
Orifice diameter	130 μm
Number of orifices	10
Fuel temperature	300 K
Injection pressure	60 bar to 120 bar

www.manaraa.com

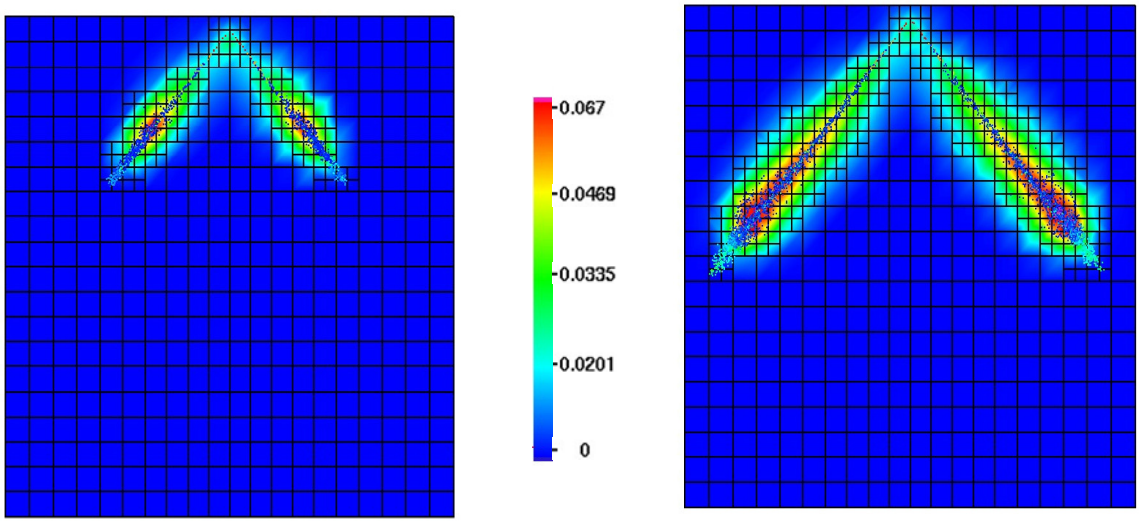

(a) 0.7 ms after spray injection (b) 1.6 ms after spray injection

Figure 3.5 Predicted drop and vapor distributions of the gasoline spray. Injection pressure, back pressure, gas density, gas temperature and orifice diameter are 100 bar, 1 bar, 1.16 kg/m^3, 300 K and 130 μm, respectively.

Figure 3.6 showed the comparison of the experimental images and predicted drop distributions for injection pressure 100 bar and back pressure 1 bar, at 0.7 ms after injection. The simulation results were in good agreement with the experimental images. The predicted droplet distribution was also satisfactory. Figure 3.7 showed the comparison at 1.6 ms after injection with the same conditions. The spray structure was well predicted using the present model.

www.manaraa.com

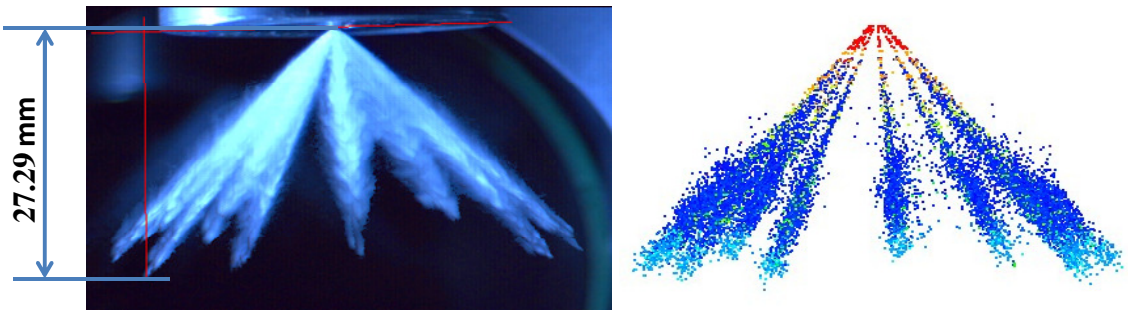

Figure 3.6 Experimental image and predicted spray structure of the gasoline spray at 0.7 ms after injection. Injection pressure, back pressure, gas density, gas temperature and orifice diameter are 100 bar, 1 bar, 1.16 kg/m^3, 300 K and 130 μm, respectively.

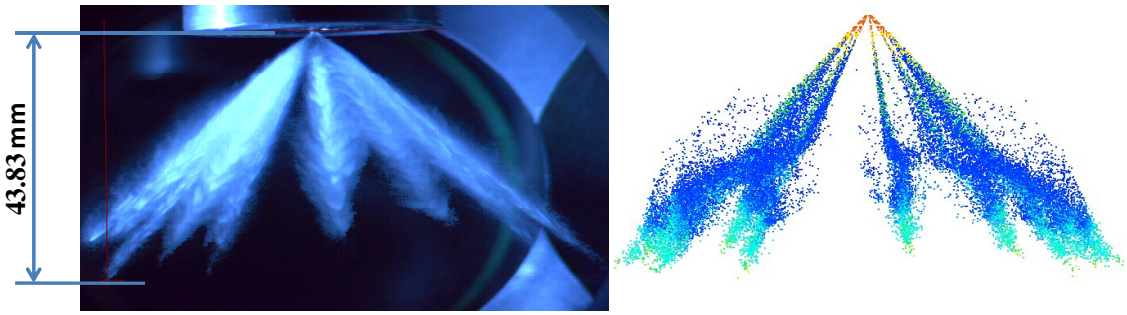

Figure 3.7 Experimental image and predicted spray structure of the gasoline spray at 1.6 ms after injection. Injection pressure, back pressure, gas density, gas temperature and orifice diameter are 100 bar, 1 bar, 1.16 kg/m^3, 300 K and 130 μm, respectively.

The effects of back pressure on the penetration of gasoline sprays were also modeled and the results were compared with the experimental data, as shown in Figure 3.8. The injection pressure was maintained constant and the back pressure was varied. The predicted penetration decreased as the back pressure increased, as also observed in the experiments. The simulation results over-predicted the penetration for one bar case by about 20 percent and were within (+/-) 5 percent for the three and five bar cases.

www.manaraa.com

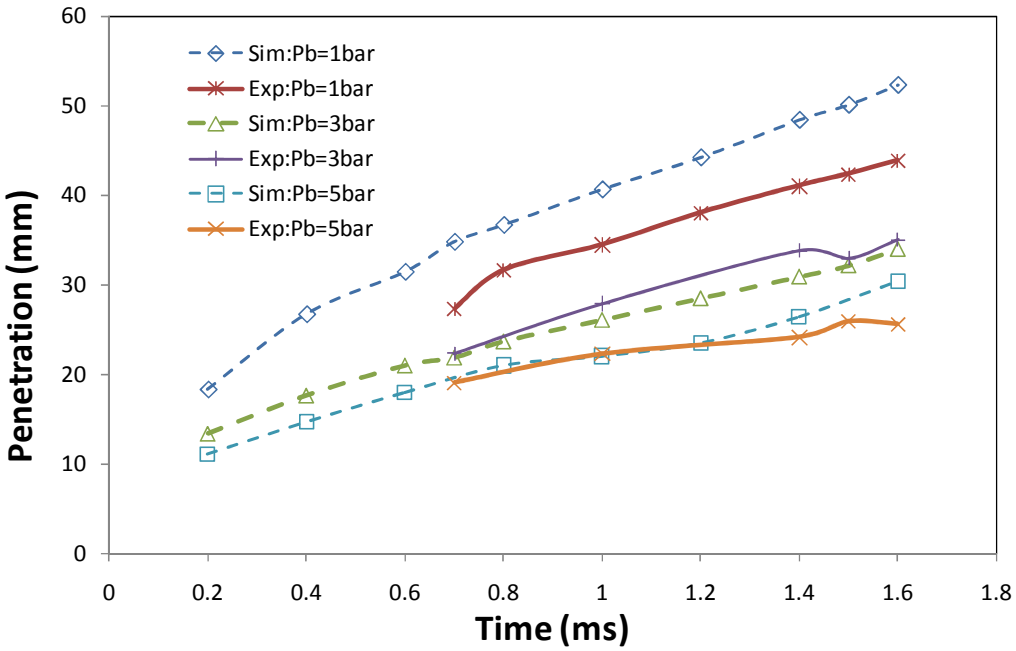

Figure 3.8 Effects of back pressure on the liquid penetration history. Injection pressure, gas density, gas temperature and orifice diameter are 100 bar, 1.16-5.78 kg/m^3, 300 K and 130 μm, respectively.

Predicted spray penetrations using different injection pressures were compared with experimental data as shown in Figure 3.9. As expected, liquid penetrations increased as the injection pressure increased. The model prediction of penetration was (+/-) 10 percent with the measurements. The model was able to predict the trend as well as the actual liquid penetration length. Overall speaking, the present primary atomization model and the hybrid KH/RT model with dynamic mesh refinement are able to predict the spray penetration and spray structure correctly.

www.manaraa.com

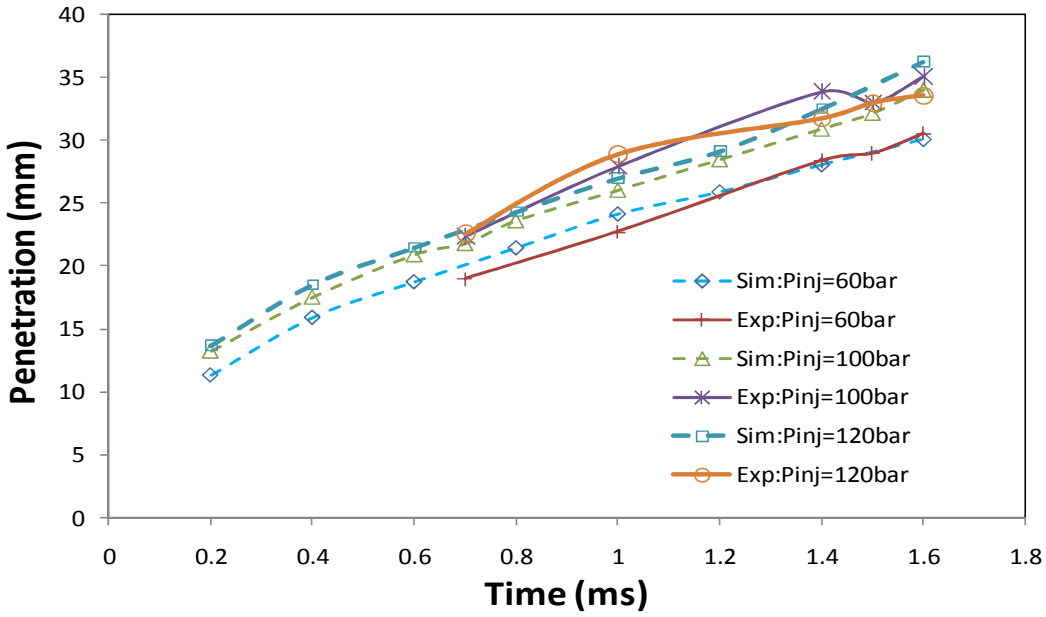

Figure 3.9 Effects of injection pressure on the liquid penetration history. Back pressure, gas temperature and orifice diameter are 3 bar, 3.47 kg/m^3, 300 K and 130 μm, respectively.

3.3.2 Diesel Spray Modeling

The model was further validated by comparing the simulation results with the experimental diesel spray data of Siebers (1998) under various conditions. The liquid length was the maximum axial penetration of the liquid phase fuel in an evaporating diesel spray. The parameters that were varied included the orifice diameter, fuel temperature, and ambient gas temperature and density. The conditions were given in Table 3.2.

www.manaraa.com

Table 3.2 Conditions for the diesel spray.

Fuel	HMN (C16H34)
Ambient gas density	3.3 to 60 kg/m^3
Ambient gas temperature	700 to 1300 K
Fuel temperature	375 to 440 K
Orifice diameter	100 to 500 μm
Orifice pressure drop	130 to 150 MPa
Number of orifices	1

The effect of the ambient gas density on the liquid length is shown in Figure 3.10. Note that the liquid penetration reached a steady-state length due to the continuous vaporization of leading drops. The simulation results showed that the liquid length decreased with increased ambient gas density since it was more difficult for drops to penetrate in a high-density environment. The model results agreed with the experimental data and were (+/-) 10 percent off the experimental results. The effect of ambient temperature on the liquid length was shown in Figure 3.11. Simulation results followed the general trend that the liquid length decreased with increased gas temperature due to high vaporization rate of liquid fuel in high-temperature environments.

www.manaraa.com

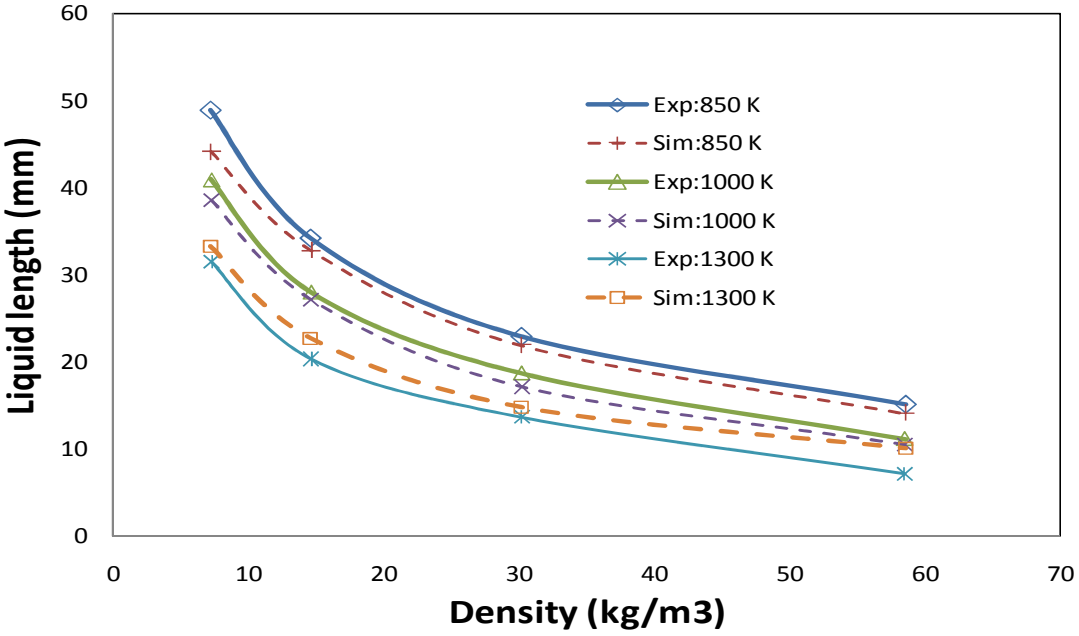

Figure 3.10 Liquid length as a function of the ambient gas density. The injection pressure, fuel temperature and orifice diameter are 136 MPa, 438 K and 246 μm, respectively.

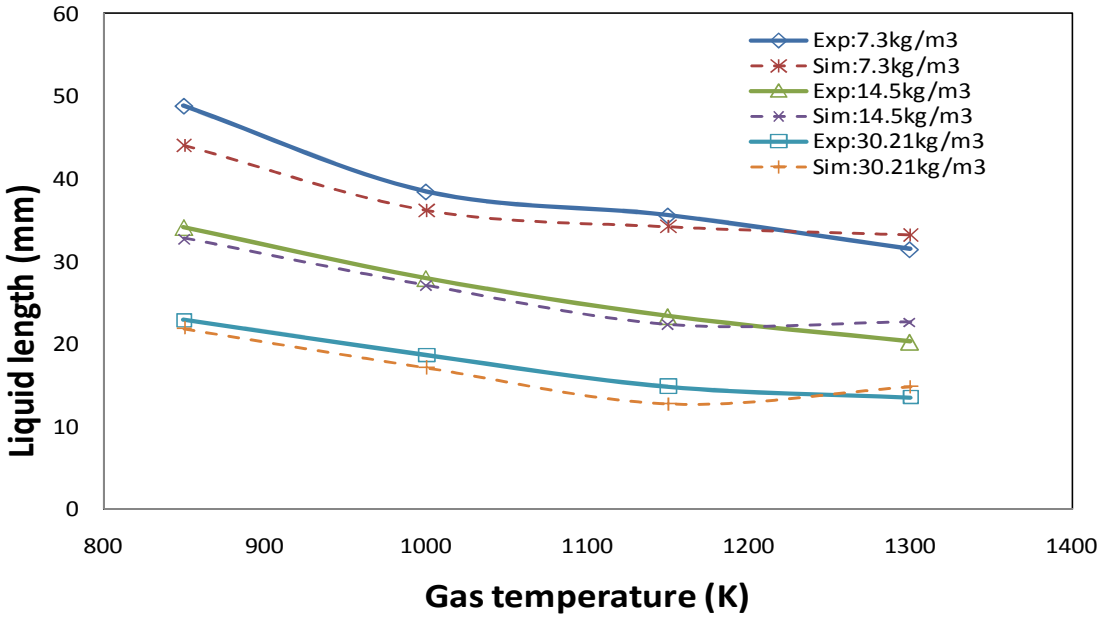

Figure 3.11 Liquid length as a function of ambient gas temperature. The injection pressure, fuel temperature and orifice diameter are 136 MPa, 438 K and 246 μm, respectively.

www.manaraa.com

Figure 3.12 shows the variation of the liquid length with the orifice diameter. The liquid length increased linearly with an increase in the orifice diameter. This was because a small nozzle hole produced small drops that could atomize and vaporize more easily. Additionally, the large drops resulting from the large orifice had higher momentum to penetrate further into the combustion chamber. In the actual diesel engine application, a smaller orifice is preferred due to its capability to produce a better fuel-air mixing to reduce soot emissions (Pickett and Siebers, 2004).

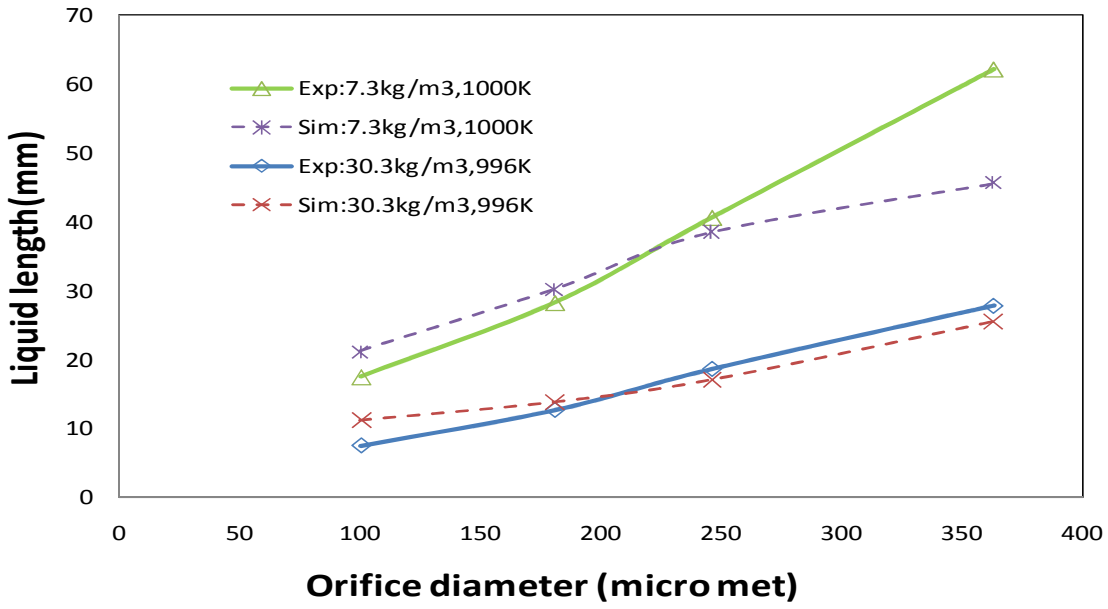

Figure 3.12 Liquid length as a function of orifice diameter. The injection pressure and fuel temperature are 135 MPa, and 438 μm , respectively.

The effect of the fuel temperature on the liquid length was also modeled and the results were compared with the experimental data as shown in Figure 3.13. The decrease in the liquid length with increased fuel temperature was predicted correctly using the present model. A high fuel temperature would enhance vaporization and thus reduce the liquid penetration. However, the effects were not significant.

www.manaraa.com

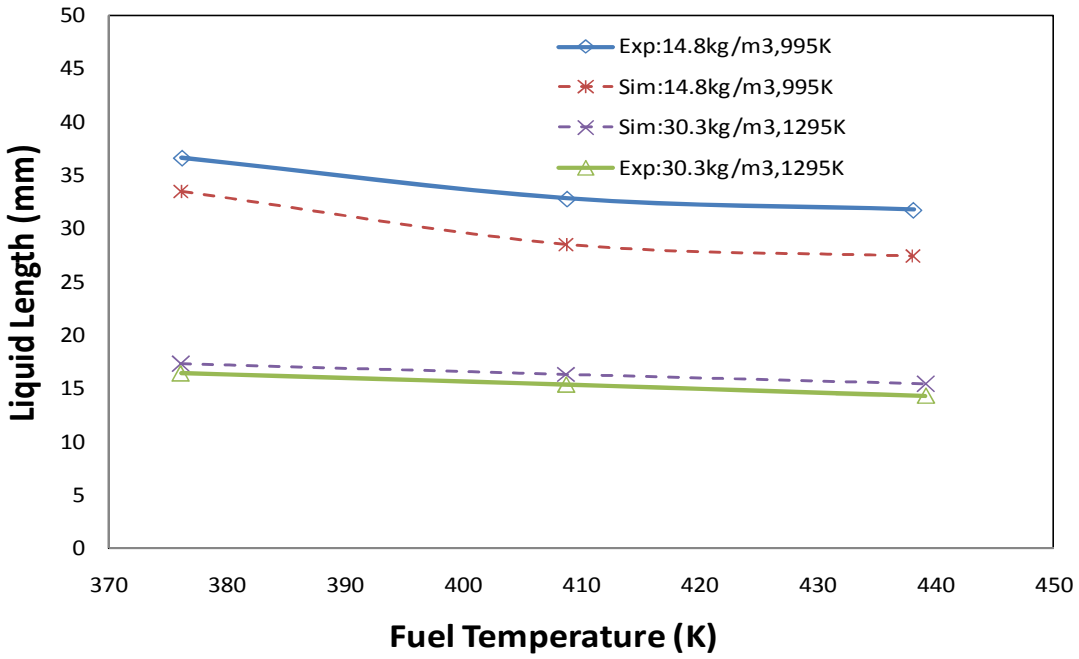

Figure 3.13 Liquid length as a function of fuel temperature. The injection pressure and orifice diameter are 135 MPa, and 246 μm , respectively.

It should be noted that traditionally the gasoline spray and diesel spray are modeled using different breakup models (Kong et al., 1999). The model by O'Rourke and Amsden (1987) has been widely used for gasoline spray breakup simulation while the KH-RT model (Patterson and Reitz, 1998) was used for diesel spray modeling. The present study used an integrated nozzle flow model and primary and secondary breakup models to simulate both gasoline and diesel sprays. Model results were in good agreement with experimental data over a wide range of condition with adjustments in model constants. Additionally, the present dynamic mesh refinement allowed using a coarse base mesh for efficient computation.

www.manaraa.com

3.3.3 Direct-Injection Gasoline Engine Modeling

The present model was applied to simulate the in-cylinder spray process in a direct-injection gasoline engine. The computational mesh was shown in Figure 3.14. The bore was 103.75 mm and the stroke was 107.55 mm. A baseline coarse mesh on this geometry had approximately 80,000 cells and a further refined mesh would be computationally expensive. Thus, it was appropriate to use a coarse mesh with dynamic mesh refinement that could provide proper grid resolution in the spray region and avoid the use of an overly fine mesh. Note that this study focused on the application of dynamic mesh refinement and spray models. Benchmark studies on computer time using different mesh densities were not performed. The speed-up obtained due to use of AMR in comparison to the fine mesh was done by comparing two grids of spatial resolution 20 x 20 x 20 and 40 x 40 x 40. The speed-up is based on the computer time of using the fine grid and defined as

$$Speed-up = \frac{Computationaltime\ \ for\ \ globally\ \ fine\ mesh}{Computational\ time}.$$

The AMR mesh shows a significant speed-up of nearly 5 times of the speed-up for solid-cone spray and 3 times of the speed-up for the hollow-cone spray. More details on the comparison of computer times using different meshes can be found in Xue and Kong (2009).

www.manaraa.com

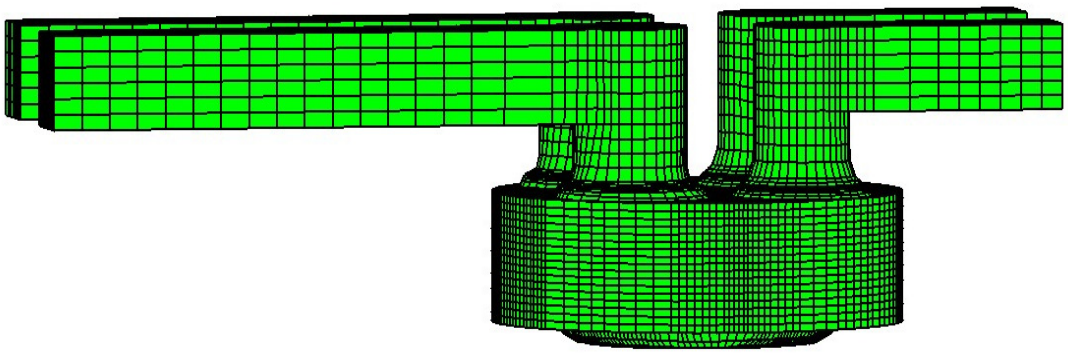

Figure 3.14 Computational mesh of the present gasoline engine.

The engine operating conditions were given in Table 3.3. Figure 3.15 showed the liquid drop distribution on two different views at two different times. The mesh and fuel vapor mass fraction on a cut-plane were also shown. The cut-plane was across two fuel jets and through the center of the cylinder. It can be seen that locally fine mesh was generated in the spray region. The present spray model and mesh refinement algorithm were applied to simulate the direct-injection gasoline spray process successfully. Further analysis of mixture distributions and validation using experimental data will require future investigations.

Table 3.3 Conditions for the present direct-injection gasoline engine.

Bore and stroke (cm)	10.375 and 10.755
Engine speed (rpm)	1000
Fuel	Gasoline
Initial gas temperature and pressure	300 K and 1 bar
Orifice diameter and fuel temperature	100 μm and 300 K
Number of orifices	6

www.manaraa.com

Computation duration	300 to 720 ATDC
Start of injection	400 ATDC
Injection duration	60 ATDC
Injected fuel mass	0.060 g/s
Averaged injection velocity(cm/s)	13500
Intake valve (open / closure)	370 / 608 ATDC
Exhaust valve (open / closure)	106 / 372 ATDC

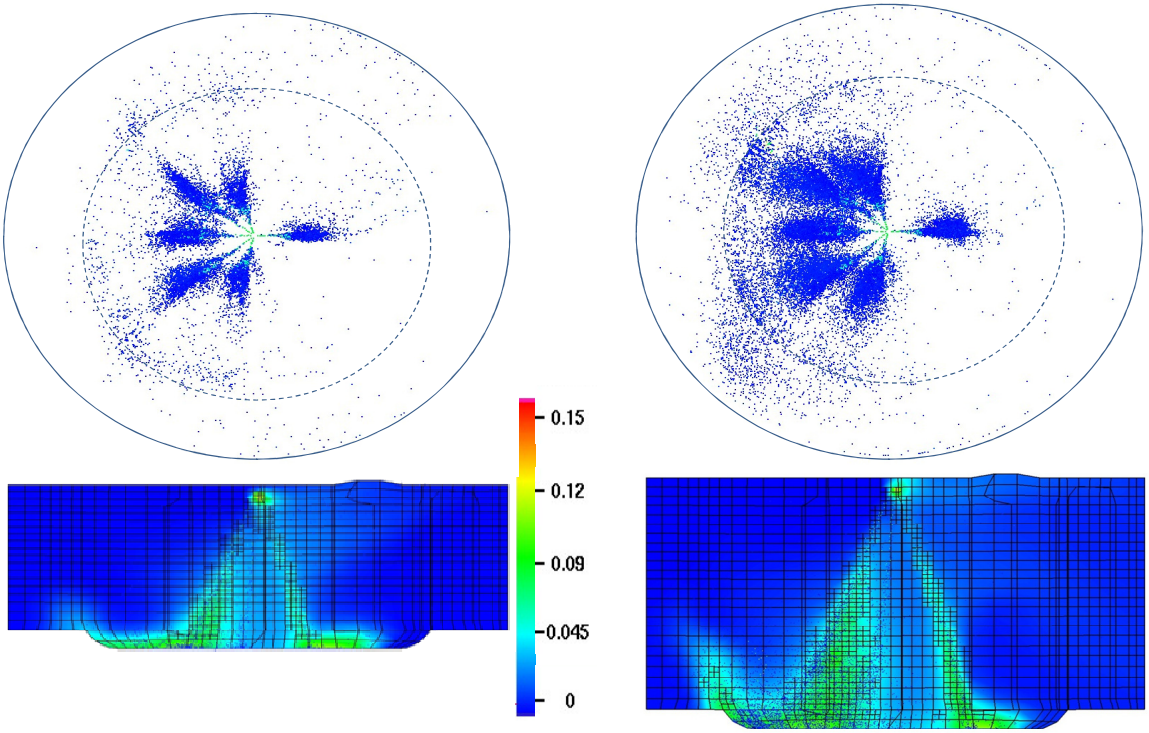

(a) 420 ATDC (b) 440 ATDC

Figure 3.15 Predicted fuel drop distributions and fuel vapor mass fraction on two views at two different times. The injection timing was 400 ATDC. The scale shown is the fuel mass fraction.

www.manaraa.com

3.4 Summary

This study implemented a nozzle flow model, a primary jet breakup model, and a secondary drop breakup model into the collocated version of KIVA-4 capable of performing dynamic mesh refinement. The model was validated using experimental data of low-pressure gasoline sprays and high-pressure diesel sprays. This study demonstrated that the present model with mesh refinement schemes can be successfully applied to engine spray simulation with satisfactory performance. The application of adaptive mesh refinement in modeling realistic engine geometries was also demonstrated in this study. The present mesh refinement scheme can allow the use of a coarse baseline mesh for computational efficiency.

www.manaraa.com

CHAPTER 4. DIESEL COMBUSTION MODELING

4.1 Introduction

In direct-injection diesel engines, the spray combustion process is a non-stationary, three-dimensional, multi-phase process that takes place in high-temperature and high-pressure environments. The development of multidimensional CFD-codes can help simulate this complex diesel combustion process and describe the real engine process by considering temporal and spatial variations of the flow field, temperature, and fuel-air composition in the combustion chamber. The use of engine CFD models to help understand the diesel combustion process has been extensive (Hergart et al., 1999; Kong et al., 2002; Kong et al., 2003; Kong et al., 2007).

Even the combustion of simple hydrocarbons, such as methane (CH_4), is a complex reaction mechanism and involves numerous intermediate species. A popular single-component surrogate for diesel fuel is n-heptane (C_7H_{16}), which is large hydrocarbon, and the reaction mechanism becomes even more complicated. The detailed reaction mechanism of the n-heptane consists of hundreds of reactions and species (Baulch et al., 1992; Chevalier, 1990). The application of these complex mechanisms to three-dimensional turbulent flows is not commonly used because of the excessive computational cost. Instead of these detailed mechanisms, reduced mechanisms with a few reactions and species can be a good alternative to reflect the combustion characteristics to a desired level of detail.

The global single-step mechanisms allow rough estimations about integral reaction and heat release rates, but they cannot provide more detailed insights into the formation and

www.manaraa.com

oxidation of intermediate species, which may be important for the formation of exhaust emissions. The quasi-global multi-step mechanisms can describe the oxidation of hydrocarbon fuels by a set of at least two or more global reactions. But these multi-step mechanisms must include the rate controlling reaction steps and characteristic intermediate species. The complex mechanisms can be reduced to simple mechanisms by identifying the rate controlling reactions and reducing it to a simpler and computationally more efficient quasi-global multi-step mechanism (Peters, 1993). It is also necessary to obtain the main reaction path by determining how much of certain species is formed by a specific reaction. Further simplification of the mechanisms can be obtained by assuming that several species are in partial equilibrium with each other because reactions between these species are extremely fast. This allows to directly solve for their concentrations, without the need of numerical integration of the differential equations describing the chemical kinetics. A prominent example for quasi-steadiness is the formation of the thermal nitrogen oxides.

In CFD calculations of internal combustion engines, one- and two-step schemes are still widely used to model the combustion process. Nevertheless, a number of on turbulent combustion in IC engines have been executed based on detailed chemistry, and improved results compared to the simpler reaction mechanisms have been reported. There are different flame regimes depending on the mixture formation and the interaction between the chemistry and turbulence. The non-premixed flames are considered in diesel engines, where the mixing of fuel and air and combustion takes place simultaneously. This is also referred to as diffusion flame, Figure 2.2 indicates the engine-related applications where the respective combustion types can be observed. The different flame types of various engine concepts may

www.manaraa.com

require different modeling approaches to appropriately describe the respective combustion phenomena.

The ignition process is mainly classified into thermal and chemical explosions. The temperature change in thermal explosion is explained by the difference in the heat production by chemical reactions and the heat loss to the surroundings. The heat loss is approximated by the Newton's law for convective heat exchange and the heat production is expressed by an Arrhenius equation for a single-step reaction from fuel to products. The heat production term increases exponentially with temperature and the heat loss changes linearly with temperature. The thermal explosion takes place depending upon the difference between the heat production and heat loss. On the other hand, chemical explosions depend on the reaction path. The associated heat release increases when there is an increase in the number of radicals in a system by chain branching reactions. The important steps involved are chain initiation (radicals are formed from stable molecules), chain propagation (radicals are conserved), chain branching (increase in the number of reactive species which cause the explosion), and chain termination.

In this chapter, the study implemented an ignition model to simulate the auto ignition of hydrocarbons and a combustion model to simulate the remaining combustion process. For modeling emissions, nitric oxide production is described by the extended Zel'dovich mechanism, and a two-step soot model was used to predict the soot emissions. The spray is modeled by the Lagrangian-drop and Eulerian-fluid technique. The fuel spray primary breakup, secondary atomization, droplet collision and the interaction of spray particles and gas are modeled using the spray model mentioned in Chapter3. Additionally, the dynamic

www.manaraa.com

mesh refinement was used to reduce the computational cost and. The overall model was validated using experimental results of a constant-volume combustion chamber and realistic diesel engines.

4.2 Model Formulation

4.2.1 Base CFD Code

The ignition, combustion and emission models were implemented into a three-dimensional CFD code KIVA-4 (Torres and Trujillo, 2006; Torres, 2007) that solves the compressible Navier-Stokes equations and have the capability of using both structured and unstructured meshes. The version of KIVA-4 used in this study is based on the "collocated" approach that assigned all cell properties at the cell center, including the velocity (Torres, 2007). The dynamic mesh refinement to save the computational cost was also implemented into the code. The details about the CFD code and dynamic mesh refinement can be found in Chapter 3 and the related references.

4.2.2 Ignition Model

The multistep Shell ignition model initially developed for the autoignition of hydrocarbon fuels at high pressures and temperatures by Halstead et al. (1977) and further extended to diesel combustion by Kong and Reitz (1993) was used for this study. This model also accounts for the "negative temperature" coefficient phenomena. The eight reaction steps between five species included in this ignition model are mentioned in Chapter 2 (Eq. 2.13 to 2.20). The reaction (Eq. 2.13) represents the chain initiation, (Eq. 2.14 to 2.17) are chain propagation reactions, Eq. 2.18 is the chain branching step and finally, Eq. 2.19 and 2.20 are

www.manaraa.com

the linear and quadratic terminations. The rate of change of the intermediate species are from Eq. 2.21 to 2.25. The rate coefficients used in the above mentioned equations are Arrhenius type,

$$f_1 = A_{f1} \exp\left(-E_{f1}/RT\right)\left[O_2\right]^{x1}\left[RH\right]^{y1}, \tag{4.1}$$

$$f_2 = A_{f2} \exp\left(-E_{f2}/RT\right), \tag{4.2}$$

$$f_3 = A_{f3} \exp\left(-E_{f3}/RT\right)\left[O_2\right]^{x3}\left[RH\right]^{y3}, \tag{4.3}$$

$$f_4 = A_{f4} \exp\left(-E_{f4}/RT\right)\left[O_2\right]^{x4}\left[RH\right]^{y4}, \tag{4.4}$$

$$k_i = A_i \exp\left(-E_i/RT\right), \tag{4.5}$$

where index i stands for $(i = 1, 2, 3, Q, B)$, and

$$k_p = \left[\frac{1}{k_1\left[O_2\right]} + \frac{1}{k_2} + \frac{1}{k_3\left[RH\right]}\right]^{-1}. \tag{4.6}$$

The kinetic parameters used in the present Shell model for diesel ignition study, can be found in Kong et al. (1995). The model uses different values for the kinetic parameter for different fuels and has the capability of predicting the ignition delay and the dependence of the ignition delay on pressure, temperature and mixture stoichiometry with reasonable accuracy.

www.manaraa.com

4.2.3 Combustion Model

In diesel spray combustion, once ignition occurs, the remaining combustion is thought to be mixing-controlled, and the interactions between turbulence and chemical reactions have to be considered. The combustion model used for this study is called laminar-and-turbulent characteristic-time combustion model (Kong et al, 1995). This model was combined with the Shell ignition model to simulate the whole combustion process in a diesel engine. The criteria is to switch the between the models at 1000K. The Shell ignition model was used to simulate the low temperature chemistry when the local temperature is less than 1000K.

The change in species density predicted by the combustion model, in terms of the characteristic time scale and the equilibrium composition, is given by

$$\frac{d\rho_i}{dt} = -\frac{\rho_i - \rho_i^{eq}}{\tau_c} = -\frac{\rho_i - \rho_i^{eq}}{\tau_l + f\tau_i} \tag{4.7}$$

Where ρ_i the density of species i, ρ_i^{eq} is the local and instantaneous thermodynamic equilibrium of the density, and τ_c is the characteristic time to achieve such equilibrium. The characteristic time is assumed to be same for all the species to predict the thermodynamic equilibrium temperature accurately. The characteristic time τ_c is approximately formulated as the sum of a laminar time scale and a turbulent time scale

$$\tau_c = \tau_l + f\tau_t. \tag{4.8}$$

www.manaraa.com

Accordingly, the delay factor f is a function of local composition r, which indicates the local completeness of combustion and varies from zero to unity for unburned and completely burned mixture given by

$$f = \left(1 - e^{-r}\right) / 0.632 \tag{4.9}$$

$$r = \frac{Y_{CO_2} + Y_{H_2O} + Y_{CO} + Y_{H_2}}{1 - Y_{N_2}} \tag{4.10}$$

The delay factor f also changes from zero to unity depending on the local conditions. The laminar timescale τ_l is derived from the correlated one-step reaction rate and is found by assuming the equilibrium concentration of fuel equal to zero. The laminar time scale is given as

$$\tau_l = A^{-1}\left[C_{14}H_{30}\right]^{0.75}\left[O_2\right]^{-1.5}\exp\left(E_A/RT\right) \tag{4.11}$$

where the pre-exponential constant and the activation energy are given by $A = 7.68.10^8$ *and* $E_A = 77.3 kJ/mol$, respectively. The turbulent time scale τ_t is proportional to the eddy turn-over time and depends upon the turbulent model used. The standard $k-\varepsilon$ turbulence model is used for this study.

$$\tau_t = 0.142k/\varepsilon \tag{4.12}$$

The initiation of combustion relies on laminar chemistry and then turbulence influences the combustion gradually. The separate effects of laminar chemistry and turbulence are to use the appearance of products as an indicator of mixing following the initiation of combustion

www.manaraa.com

events. The amount of heat release can be estimated based on the respective enthalpies of formation of the species involved i and the change rates of the various species densities

$$\frac{dQ_{ch}}{dt} = -\sum_i \frac{d\rho_i}{dt}\frac{1}{MW_i}\tilde{h}^0_{f,i} \tag{4.13}$$

4.2.4 NOx Model

The modeling of thermal nitric oxide (NO) is described by the extended Zel'dovich mechanism (Patterson et al., 1994; Kong et al., 1995). The extended Zel'dovich mechanism consists of the following equations (Bowman, 1995):

$$O + N_2 \underset{k_{1b}}{\overset{k_{1f}}{\rightleftharpoons}} NO + N \tag{4.14}$$

$$N + O_2 \underset{k_{2b}}{\overset{k_{2f}}{\rightleftharpoons}} NO + O \tag{4.15}$$

$$N + OH \underset{k_{3b}}{\overset{k_{3f}}{\rightleftharpoons}} NO + H \tag{4.16}$$

The above equations are solved by assuming a steady state population of N and assuming Eq. 4.17 in equilibrium

$$O + OH \underset{k_{4b}}{\overset{k_{4f}}{\rightleftharpoons}} O_2 + H \tag{4.17}$$

Eq. 4.14 initiates the overall mechanism by production of nitrogen atoms and proceeds only at high temperatures. Considerable amount of thermal NO are produced in the hot products regions, where the gas temperatures are well above 2000 K. A single rate equation for NO can be written using the extended Zel'dovich mechanism as,

www.manaraa.com

$$\frac{d[NO]}{dt} = 2k_{f1}[O][N_2]\left\{\frac{1-[NO]^2/K_{12}[O_2][N_2]}{1+k_{1b}[NO]/\left(k_{2f}[O_2]+k_{3f}[OH]\right)}\right\} \tag{4.18}$$

where $K_{12} = \left(k_{1f}/k_{1b}\right)\bullet\left(k_{2f}/k_{2b}\right)$ and N_2, O, O_2 and OH are assumed to be in local thermodynamic equilibrium. The rate constants are given as:

$$k_{1f} = 7.6\times10^{13}\exp\left[-38000/T\right]cm^3/\left(mol\ s\right) \tag{4.19}$$

$$k_{1b} = 1.6\times10^{13}\ cm^3/\left(mol\ s\right) \tag{4.20}$$

$$k_{2f} = 6.4\times10^{9}\exp\left[-3150/T\right]cm^3/\left(mol\ s\right) \tag{4.21}$$

$$k_{2b} = 1.5\times10^{9}\exp\left[-19500/T\right]cm^3/\left(mol\ s\right) \tag{4.22}$$

$$k_{3f} = 1.0\times10^{14}\ cm^3/\left(mol\ s\right) \tag{4.23}$$

$$k_{3b} = 2.0\times10^{14}\exp\left[-23650/T\right]cm^3/\left(mol\ s\right). \tag{4.24}$$

The kinetic reaction rate of the equations shows close dependence with the temperature, hence, the NO prediction quantity is closely coupled to the prediction quality of the heat release profile.

4.2.5 Soot Model

The soot formation is modeled by a two-step formation and oxidation model (Hiroyasu, 1989). Which is formulated by is kinetically controlled two step process written in a single step Arrhenius form. The rate of change of soot mass is equal to (Belardini et al., 1992).

www.manaraa.com

$$\frac{dM_s}{dt} = \frac{dM_{sf}}{dt} - \frac{dM_{so}}{dt}. \tag{4.25}$$

The first term on the right-hand side of Eq.4.25 denotes the soot formation (Hiroyasu, 1989) given by

$$\frac{dM_{sf}}{dt} = A_f m_{f,v} p^{0.5} \exp\left[-\frac{E_{s,f}}{RT}\right] \tag{4.26}$$

where $m_{f,v}$ is the mass of vaporized fuel mass, p is the pressure in bar, A_f is equal to 450 and $E_f = 125000\left(cal/mol\right)$. The second term on the right-hand side of Eq. 4.25 denote the soot oxidation (Nagle and Strickland-Constable, 1962) given by

$$\frac{dM_{so}}{dt} = \frac{MW_c}{\rho_s D_s} M_s R_{tot} \tag{4.27}$$

where MW_c is the molecular weight of carbon, ρ_s is the soot density $(2\ g/cm^3)$, D_s is the soot diameter $(3\times10^{-6}cm)$, and R_{tot} denotes the total soot oxidation rate given by

$$R_{tot} = \left[\frac{k_A p_{O2}}{1+k_z p_{O2}}\right] x + k_B p_{O2}\left(1-x\right). \tag{4.28}$$

Where p_{O2} is the partial pressure of oxygen in atm, and x is the ratio of more reactive sites versus less reactive sites on the soot particle due to surface variation and is given by

$$x = \frac{p_{O2}}{P_{O2} + \left(k_T/k_B\right)}. \tag{4.29}$$

The rate constants used in Eq. 4.28 and 4.29 given by Nagle and Strickland are

www.manaraa.com

$$k_A = 20\exp(-30000/RT) \tag{4.30}$$

$$k_B = 4.46\times10^3\exp(-15200/RT) \tag{4.31}$$

$$k_T = 1.51\times10^5\exp(-97000/RT) \tag{4.32}$$

$$k_Z = 21.3\exp(4100/RT) \tag{4.33}$$

The above soot mechanism has been widely used in many CFD combustion studies. The set of empirical parameters contained in the equations can be properly adjusted to specific engine conditions.

4.3 Results and Discussion

4.3.1 Sandia Constant-Volume Combustion Chamber

The model was validated using experimental data obtained in the Sandia combustion chamber (Pickett and Siebers, 2004). These experiments were conducted in a constant-volume combustion chamber under simulated diesel engine conditions. High-temperature and high-pressure environments were created by burning a specified premixed mixture before the start of fuel injection. The experimental conditions are given in Table 4.1.

Table 4.1 Experimental conditions for Sandia combustion chamber.

Fuel	#2 Diesel
Ambient gas density	7.3, 14.8, 30.0 kg/m^3
Ambient gas temperature	850 - 1300 K
Fuel temperature	436 K
Orifice diameter	100 μm

www.manaraa.com

Orifice pressure drop	138 MPa
Number of orifices	1
Injection system	Common-rail
Injection profile	Top-hat
Discharge coefficient	0.80
O_2 concentration	21%

The computational domain for the simulations was a constant-volume cylindrical chamber with 100 mm in diameter and 100 mm in height, as show in Figure 3.3. The mesh size was 5 mm before cell refinement. The ambient temperature, pressure and species concentration are similar to those of the experimental conditions.

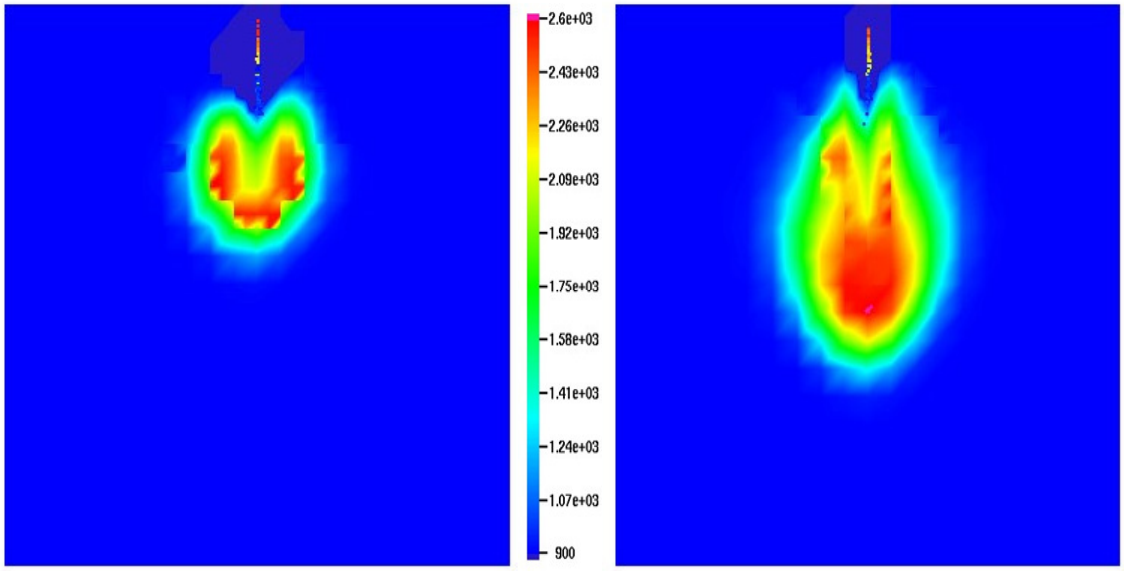

(a) 1.4 ms ASI (b) 2.7ms ASI

Figure 4.1 Predicted temperature distribution and fuel spray. The conditions are $P_{amb} = 138\,\text{MPa}, T_{amb} = 900\,\text{K}, d_{nozz} = 100\,\mu\text{m}$ and $\rho_{amb} = 14.8\,\text{kg/m}^3$.

www.manaraa.com

The two images in Fig. 4.1 show the gas temperature distributions at different times after start of injection (ASI). The ignition location is where the flame is stabilized and it is also the flame lift-off location. The lift-off length is the distance from the fuel injection point to the initiation of the stabilized flame. The length decreases with increase in temperature. The images clearly show the lift-off location of the flame. The chemical reactions before the lift-off location, where successive ignition events of the incoming fuel-air mixture occur, are significant in the stabilization of flame.

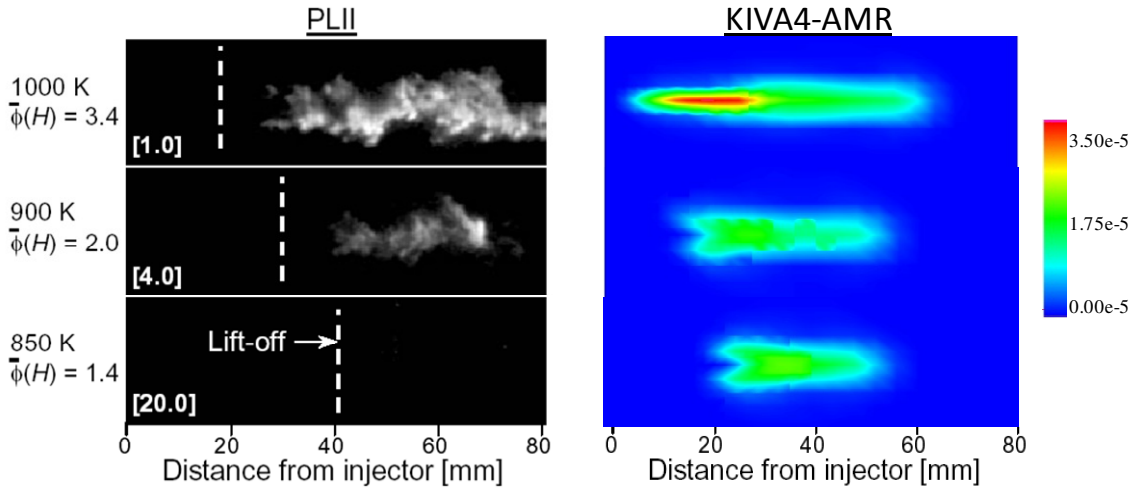

(a) Experimental PLII images (b) Predicted soot mass fraction.

Figure 4.2 Comparison of PLII images with the predicted soot mass-fractions. The plane shown is through the centre of the domain. The conditions are $d_{nozz} = 100\,\mu m$, $P_{inj} = 138\,MPa$, $\rho_{amb} = 14.8\,kg/m^3$.

The left image in Figure 4.2 shows the Planar laser-induced incandescence (PLII) images of soot along the thin plane of the fuel jet. The injector is located at the far left center of the images and the fuel is injected to the right. The right image of Figure 4.2 shows the simulation results of soot mass fraction distributions. The location of injector in the simulations are same as that in the experiments. The comparison of soot mass fraction

www.manaraa.com

distributions of PLII images and the simulations gives a reasonable match. However, the model predicted a shorter lift-off length. The experimental images and the simulations shows the increase in the lift-off length and decrease in soot production with decrease in ambient temperature.

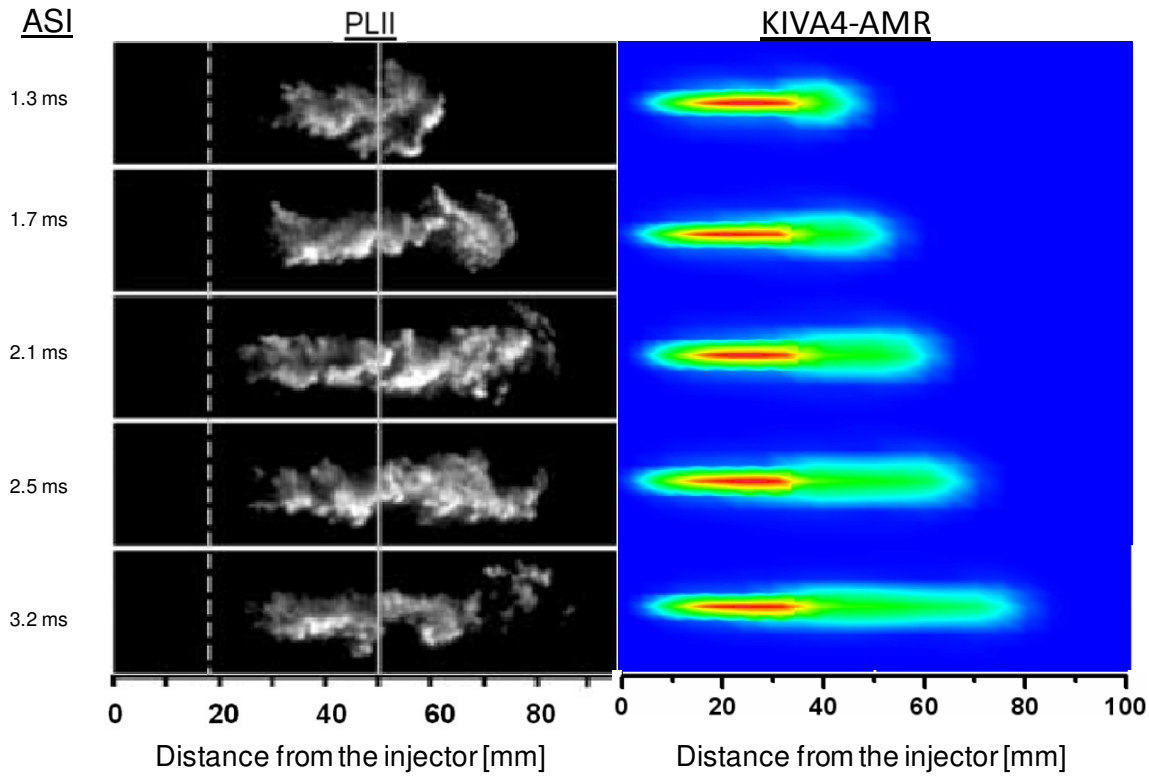

Figure 4.3 Comparison of temporal variation of PLII images with the predicted soot mass-fractions. The plane shown is through the centre of the domain. The conditions are $d_{nozz} = 100\,\mu m$, $P_{inj} = 138\,MPa$, $\rho_{amb} = 14.8\,kg/m^3$, $T_{amb} = 1000K$.

Figure 4.3 shows the comparison of the temporal variation of the soot mass distributions at different times after the start of injection. The models under-predicted the lift-off length and over-predicted the soot mass fractions.

www.manaraa.com

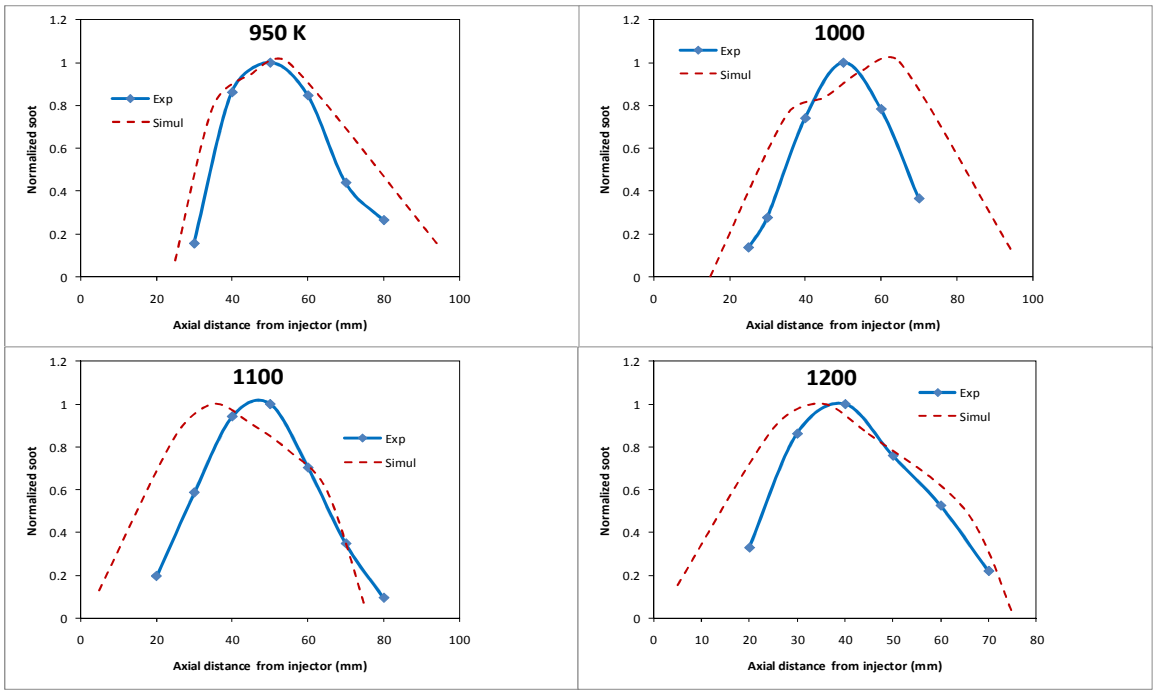

Figure 4.4 Comparison of measured time-averaged KL factors and predicted soot mass fraction, both experimental and predicted results are normalized. The results are for different ambient temperatures $950\,\mathrm{K}, 1000\,\mathrm{K}, 1100\,\mathrm{K}$ and $1200\,K$ at ASI 3.2 ms $d_{nozz} = 100\,\mu\mathrm{m}$, $P_{inj} = 138\,\mathrm{MPa}$, $\rho_{amb} = 14.8\,\mathrm{kg/m^3}$.

The KL factor is an indication of the optical thickness obtained from the laser-extinction soot measurements (Pickett and Siebers, 2004). The KL factor is also proportional to the mass of soot along the line of sight of the extinction measurement, hence, it can be compared with integrated soot mass of the simulations along the same plane. The measured KL factors and integrated soot mass fractions of the simulations are normalized to give a good comparison. The four plots in Figure 4.4 shows the comparison of the axial distribution of measured KL factors and the predicted normalized soot mass fraction at ambient temperatures of 950 K, 1000 K, 1100 K and 1200 K. The simulation results follows the same trend as the measured KL factors but, were 10 to 20 percent over and under predicting at some points.

www.manaraa.com

4.3.2 Caterpillar Heavy-Duty Diesel Engine

Further validation of the present model is performed on a heavy-duty diesel engine by simulating combustion and emissions processes. The computational mesh for the suimulation was shown in Figure 4.5. The experimental conditions and engine specifications are given in Table 4.2 and Table 4.3.

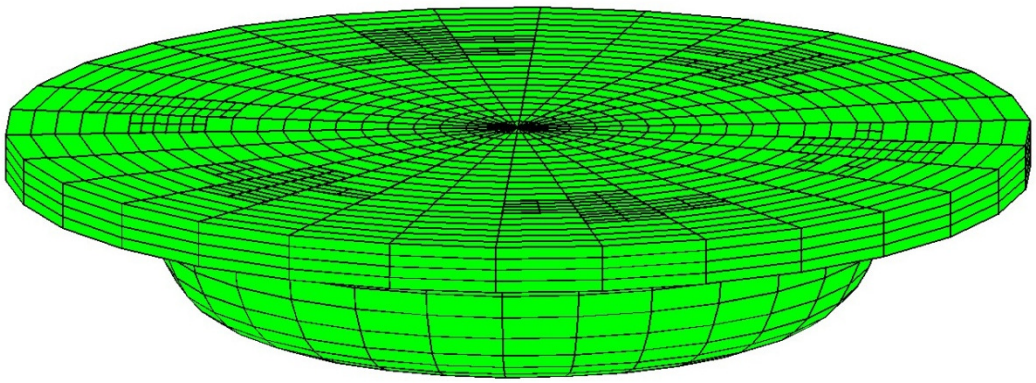

Figure 4.5 Computational mesh of the Caterpillar engine

Table 4.2 Experimental conditions.

Engine load (%)	High load (75) - Single injection	High load (75) – Double injection
Injection pressure (MPa)	90	90
Engine speed (rpm)	1600	1600
SOI	-1, +2, +5	-7, -4, -1, +2, +5
EGR (%)	0	0

www.manaraa.com

Table 4.3 Caterpillar engine specifications.

Bore X Stroke (mm)	137.2 X 165.1
Connecting rod length (mm)	261.6
Displacement volume (L)	2.44
Compression ratio	15.1
Number of nozzles	6
Nozzle diameter (mm)	0.259
Spray angle (degree)	27.5
Piston crown	Mexican hat
Combustion chamber	Quiescent
Swirl ratio	1.0
Inlet air temperature (K)	361.40
Inlet air pressure (bar)	2.08

The experimental conditions used for model validation are high load cases with both single injection and double injections at different start of injection. The computational domain is a cylindrical mesh with an average cell size of 15, 5, 0.5 mm in the direction, respectively. Measured cylinder pressure and the heat release rate are compared with the predicted values. Figure 4.6, 4.7 and 4.8 show the measured and computed cylinder pressure and heat release rate data for single injection cases, and Figure 4.8 to 4.13 for double injection cases. The computed results are in good agreement with the measured data. The model over predicted the cylinder pressure about 5 percent that of the experimental data.

www.manaraa.com

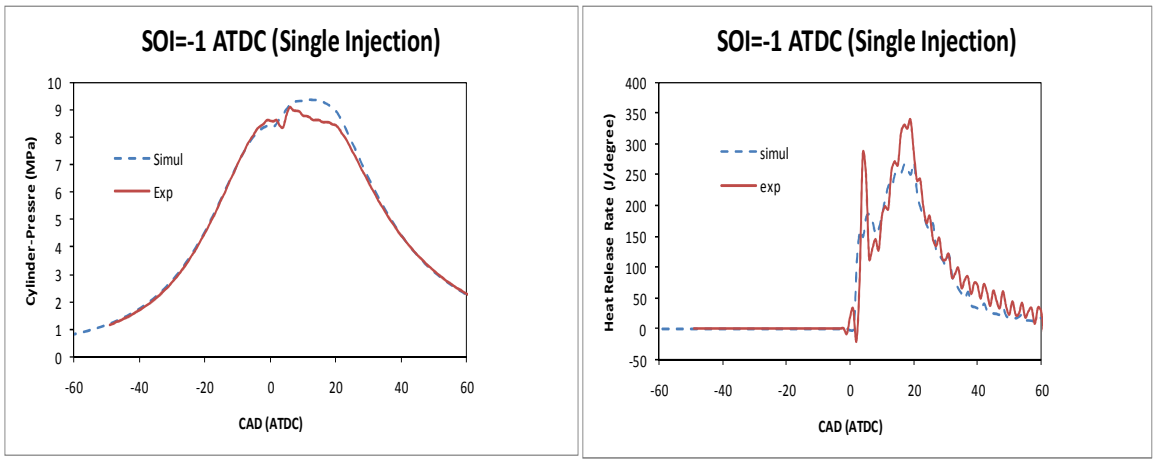

Figure 4.6 Comparison of cylinder pressure and heat release rate for high-load, single injection case for SOI = -1 ATDC.

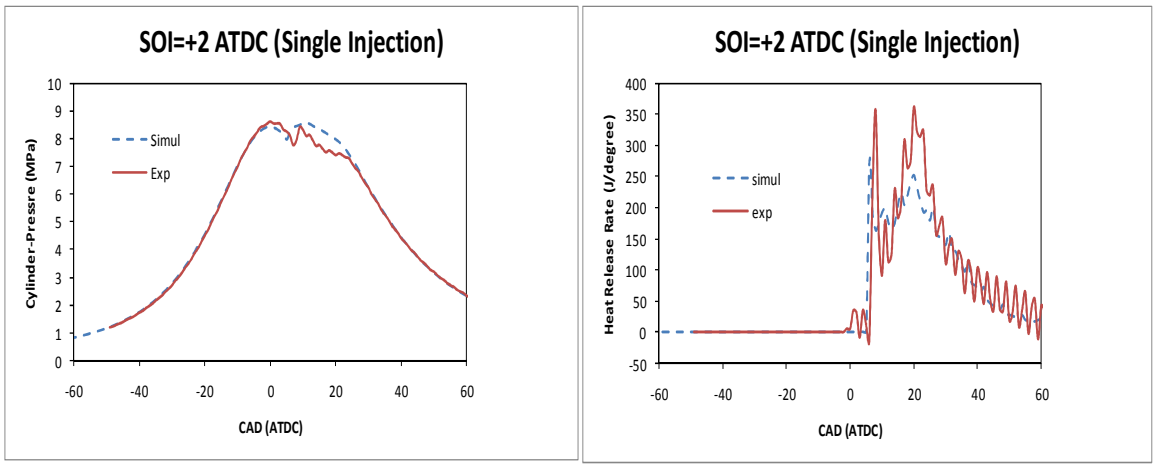

Figure 4.7 Comparison of cylinder pressure and heat release rate for high-load, single injection case for SOI = +2 ATDC.

www.manaraa.com

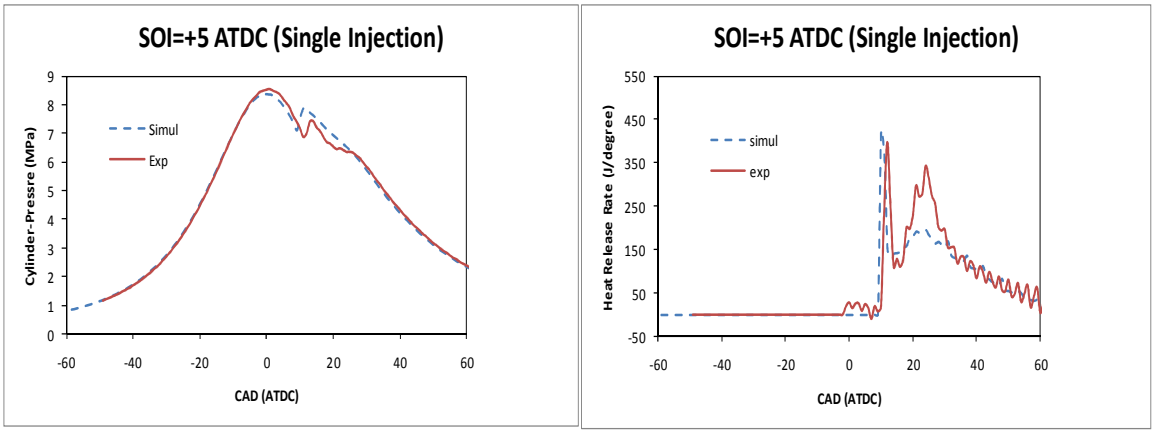

Figure 4.8 Comparison of cylinder pressure and heat release rate for high-load, single injection case for SOI = +5 ATDC.

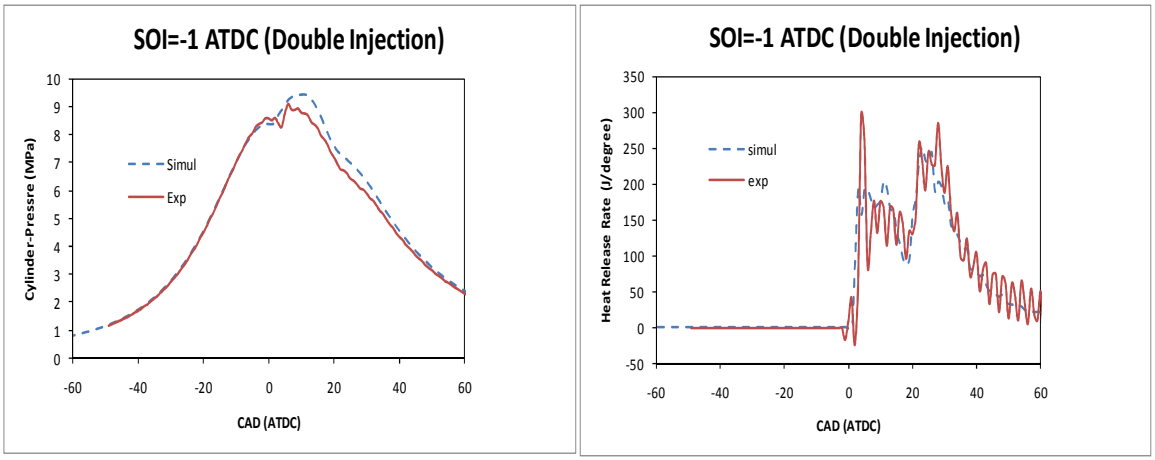

Figure 4.9 Comparison of cylinder pressure and heat release rate for high-load, double injection case for SOI = -1 ATDC.

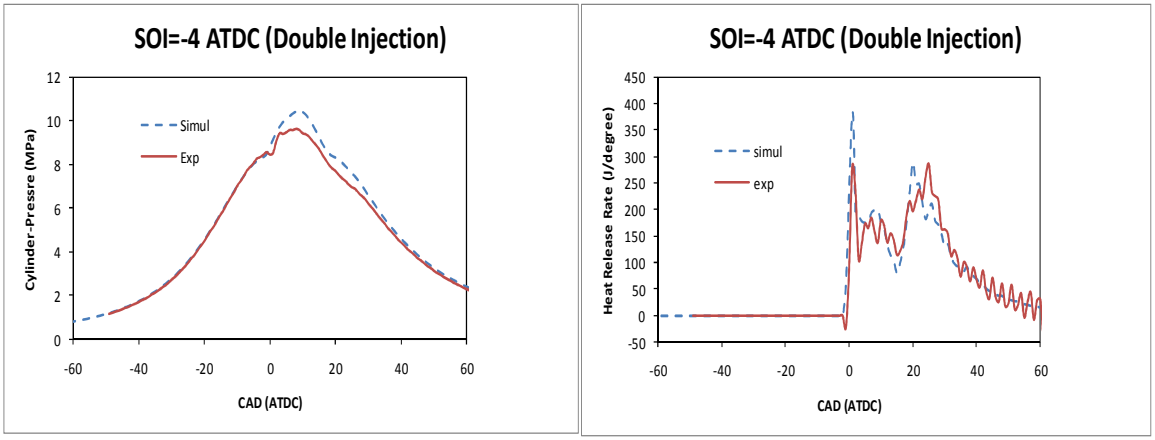

Figure 4.10 Comparison of cylinder pressure and heat release rate for high-load, double injection case for SOI = -4 ATDC.

www.manaraa.com

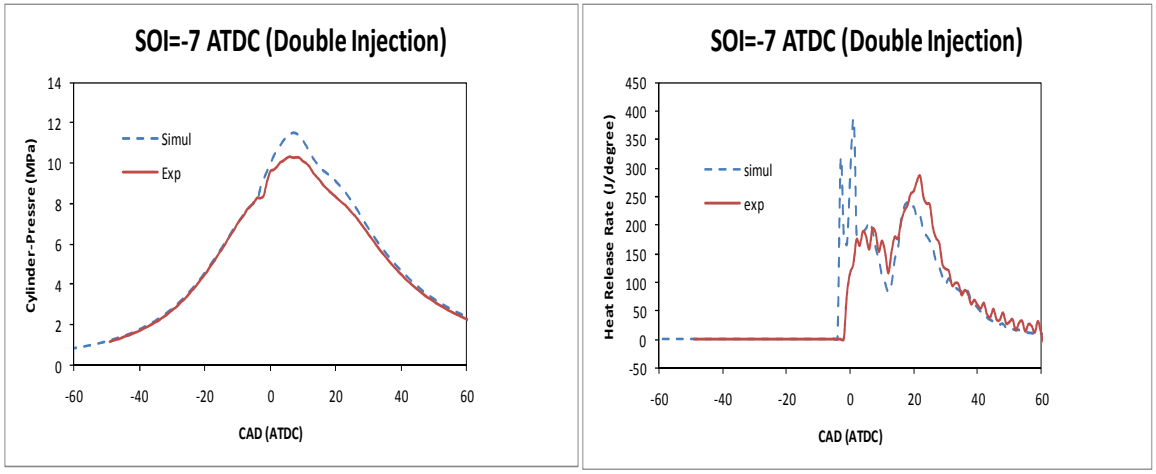

Figure 4.11 Comparison of cylinder pressure and heat release rate for high-load, double injection case for SOI = -7 ATDC.

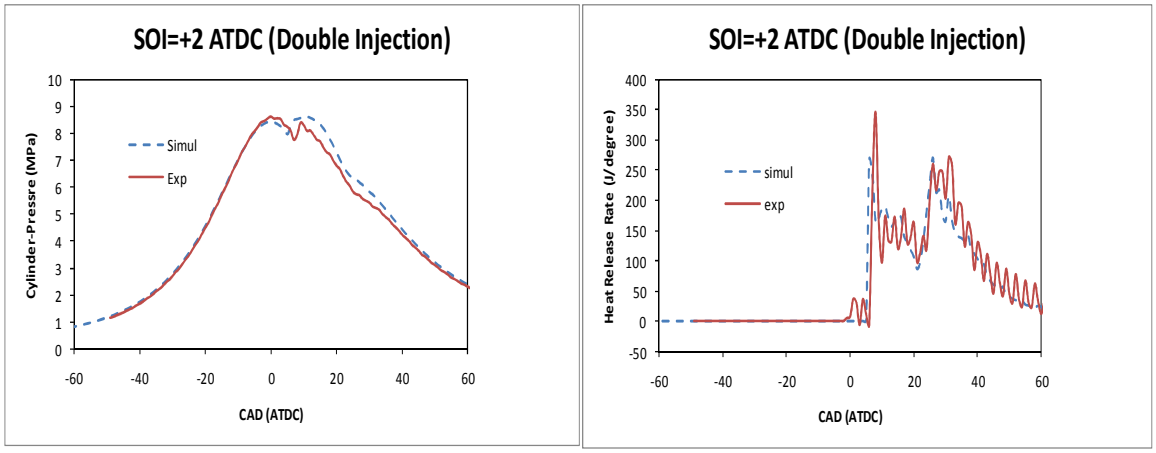

Figure 4.12 Comparison of cylinder pressure and heat release rate for high-load, double injection case for SOI = +2 ATDC.

www.manaraa.com

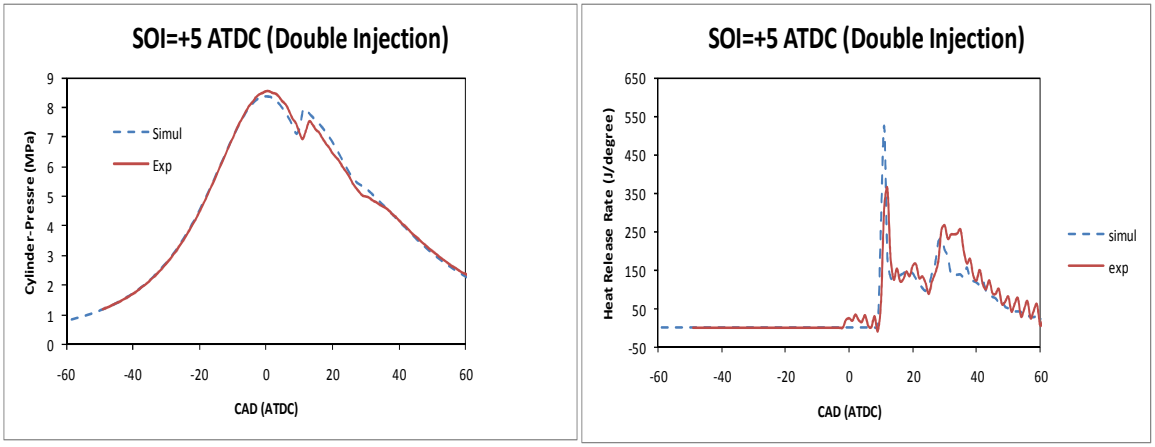

Figure 4.13 Comparison of cylinder pressure and heat release rate for high-load, double-injection case for SOI = +5 ATDC.

The predicted soot and NOx emissions were also compared with the measured data. Figure 4.14 and 4.15 show the variation of NOx and soot emissions with respect to the start-of-injection timing. In the case of NOx, the model is able to maintain the trend, but is over predicting the NOx emissions in the case of early SOI. There is good match of soot emissions between the measured and computed results. The NOx and soot prediction of the models were varying away from the experimental results by 5 to 30 percent.

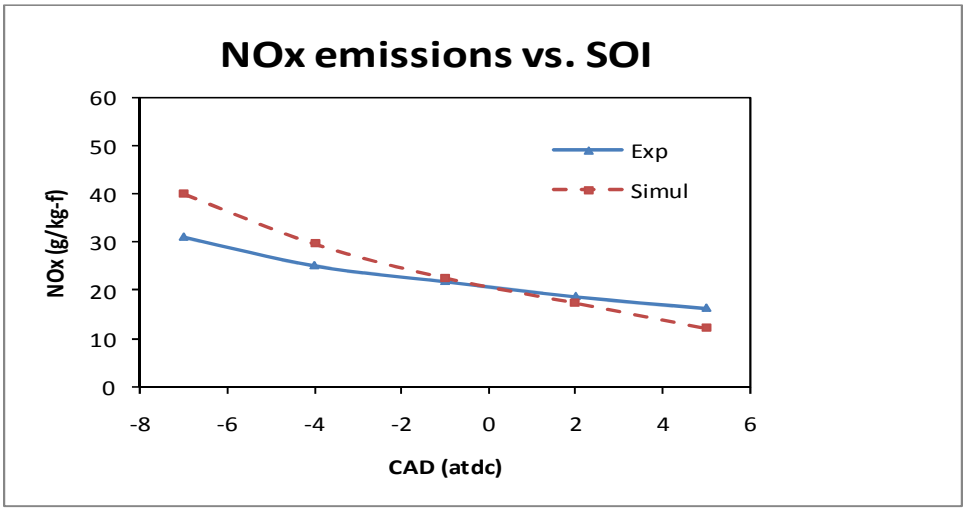

Figure 4.14 Comparision of NOx emissions with start of injection timing for the high-load double-injection cases.

www.manaraa.com

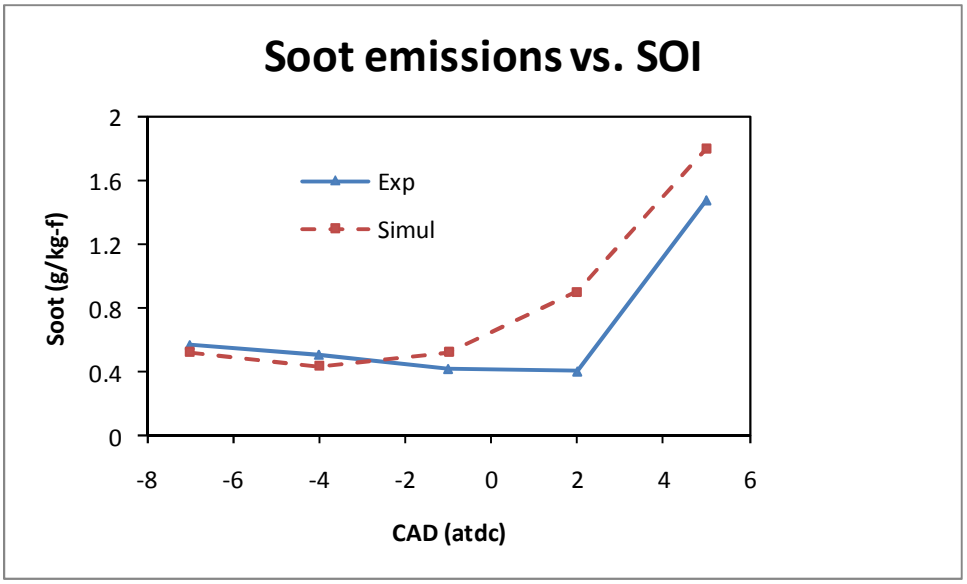

Figure 4.15 Comparision of soot emissions with start of injection timing for the high-load double-injection cases.

The computational results shown further are for SOI at -1 ATDC. The fuel drop distributions at 10 CAD after SOI is shown in Figure 4.16. Figure 4.17 showed the temperature distribution on two different views at two different times. The cut-plane was across two fuel jets through the centre of the computational domain. Figure 4.18 showed the fuel vapor mass fraction distribution on the same cut-plane at two different times.

www.manaraa.com

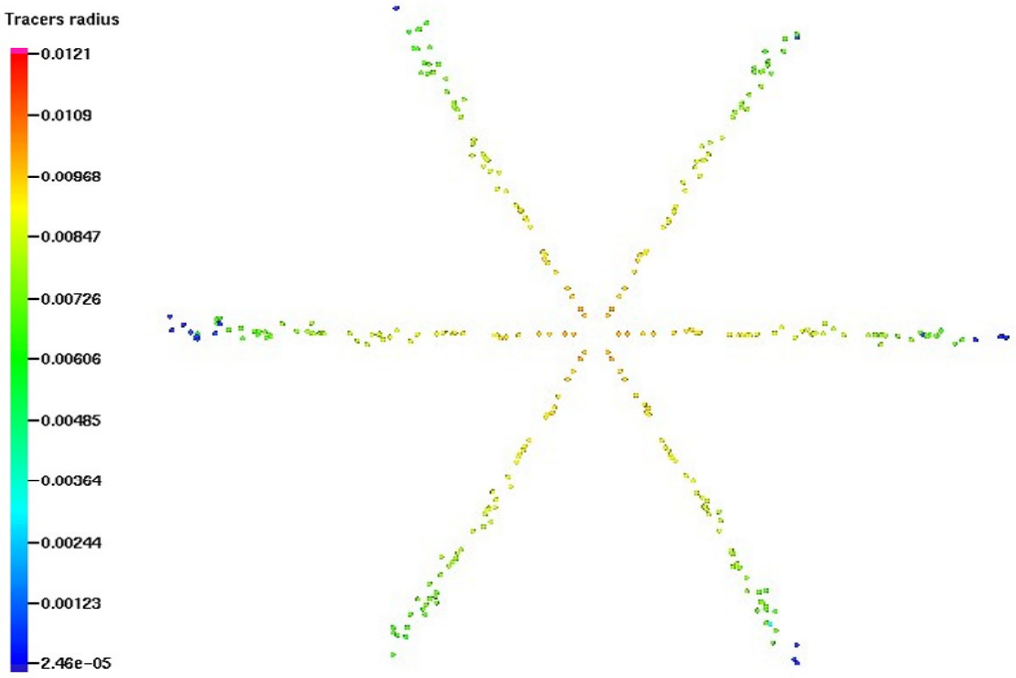

Figure 4.16 Fuel drop distributions at 10 CAD after SOI and the scale shows the droplet radius in mm.

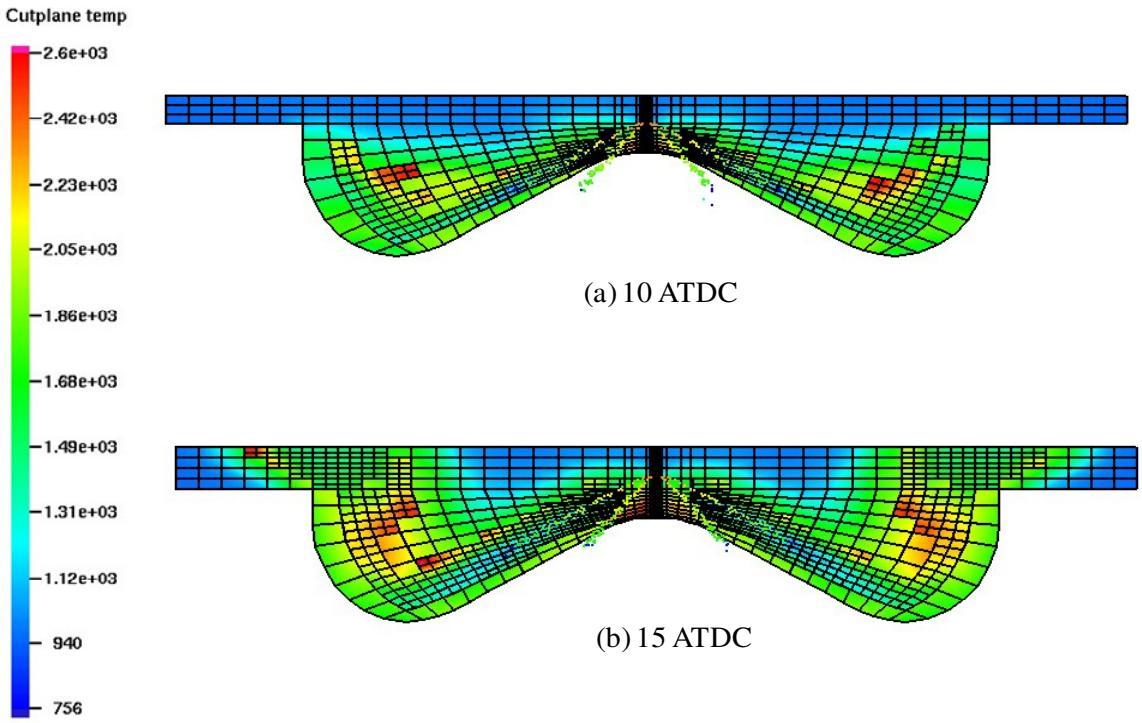

(a) 10 ATDC

(b) 15 ATDC

Figure 4.17 Temperature distributions on two views at two different times.

www.manaraa.com

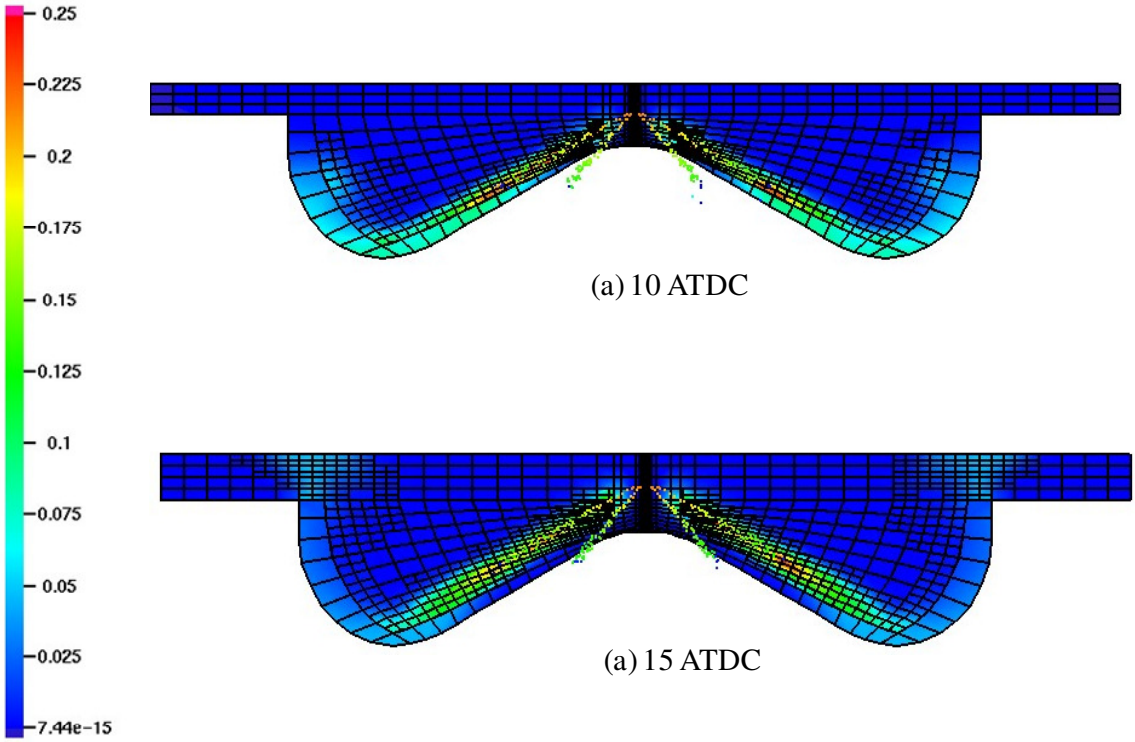

(a) 10 ATDC

(a) 15 ATDC

Figure 4.18 Fuel vapor mass fraction distributions on two views at two different times.

4.4 Summary

This study implemented an ignition model, combustion model, soot model and thermal NOx model into the collocated version of KIVA-4 capable of performing dynamic mesh refinement. The model was validated using experimental data of high-pressure diesel sprays in the Sandia combustion chamber. The PLII images of soot along the thin plane of the fuel jet were compared with the predicted soot mass fraction distributions. The model was also validated using the experimental results of a heavy-duty diesel engine, for in-cylinder pressure, heat release rate, and Soot and NOx emissions. This study demonstarted that the present model with mesh refinement schemes can be used to predict the engine combustion and emission process with satisfactory performance. The present model based on

www.manaraa.com

mesh refinement scheme allow one to use a coarse mesh to predict the combustion and emission process with reasonable accuracy and a slight increase in computational resources compared to those using the coarse mesh.

www.manaraa.com

CHAPTER 5. CONCLUSIONS

5.1 Conclusions

The collocated version of KIVA-4 capable of performing dynamic mesh refinement was improved further by implementing the spray and combustion models. The unified spray model, which is a combination of a nozzle flow model, a primary jet breakup model, and a secondary breakup model, was used to simulate both the low-pressure gasoline sprays and high-pressure diesel sprays. The comparison of simulation results with experimental data indicated good levels of agreement in liquid penetration and spray structure under various operating conditions. The model predicted correctly the liquid penetration history of the present gasoline spray for different injection pressures and ambient pressures. In the diesel spray validation, the model was also able to capture the effects of various parameters on the liquid penetration including ambient gas temperature and density, injection pressure, fuel temperature, and nozzle diameter.

The chemistry model, which is a combination of an ignition model, laminar-and-turbulent characteristic-time combustion model, and emission models, was used to simulate the combustion of diesel sprays. Initially, the model was validated by comparing the soot mass fraction distributions with PLII images of soot, and reasonable agreement was obtained. The comparison of measured KL factors and the integrated soot mass fractions of the simulations also gave a good level of agreement. The model was further validated by comparing the in-cylinder pressure and heat release data of a diesel engine. The model also

www.manaraa.com

predicted the soot and NOx reasonably well when compared with the measured data. The present model and numerical schemes can further be applied to predict engine performance under new operating conditions and help with the engine design and development.

5.2 Contributions

The development of a Unified spray model had been done, which can be applied to both low-pressure gasoline sprays and high-pressure diesel sprays. Traditionally, diesel and gasoline sprays are modeled with different models. The model consists of a nozzle flow model, primary breakup model, and secondary breakup to include all the sub process involved in spray atomization. Dynamic mesh refinement algorithm adapted to spray was also implemented in the model to reduce computational cost, which is a primary issue in modeling realistic engine geometries. The application of this model was also successfully implemented on realistic engine geometry.

An ignition, combustion, soot, and NOx model were also implemented in the Unified spray model to simulate the low and high temperature combustion chemistry in diesel engines. The model was also validated with the experimental conducted on a heavy-duty diesel engine. Finally, a model was developed which includes all the spray sub processes and combustion with dynamic mesh refinement to reduce the computational cost.

www.manaraa.com

REFERENCES

Abraham, J., 1997. What Is Adequate Resolution in the Numerical Computation of Transient Jets? SAE Paper 970051.

Arcoumanis, C., Gavaises, M., French, B., 1997. Effect of Fuel Injection Process on the Structure of Diesel Sprays. SAE Paper 970799.

Baulch, D.L., Cobos, C.J., Cox, R.A., Frank, P., Hayman, G., Just, T., Kerr, J.A., Murrells, T., Pilling, M.J., Troe, J., Walker, R.W., Warnatz, J., 1992. Evaluated Kinetic Data for Combustion Modeling. J. Phys. Chem. Ref. Data, Vol. 21, pp 411-429.

Baumgarten, C., 2006. Mixture Formation in Internal Combustion Engines. Springer-Verlag Berlin Heidelberg.

Beale, J.C., Reitz, R.D., 1999. Modeling Spray Atomization with the Kelvin-Helmholtz/Rayliegh-Taylor Hybrid Model. Atomization and Sprays,Vol.9, 623-650.

Beard, P., Duclos, J.M., Habchi, C., Bruneaux, G., Mokkadem, K., Baritaud, T., 2000. Extension of Lagrangian-Eulerian Spray Modeling: Application to High Pressure Evaporating Diesel Sprays. SAE paper 2000-01-1893.

Beck, J.C., Watkins, A.P., 2004. The Simulation of Fuel Sprays Using the Moments of the Drop Number Size Distribution. Int. J. Engine Res., vol 5, no 1, 1–21.

Belardini, P., bertoli, C., Ciajolo, A., D'Anna, A. and Del Giacomo, N., 1992. Three-Dimensional Calculations of DI Diesel Engine Combustion and Comparison with In-Cylinder Sampling Valve Data. SAE Paper 92225.

Bell, J., Berger, M.J., Saltzman, J., Welcome, M., 1994. Three-dimensional adaptive

www.manaraa.com

mesh Refinement for Hyperbolic Conservation Laws. SIAM J. Sci. Comput., 15, 127-138.

Biswas, R., Strawn, R.C., 1998. Tetrahedral and Hexahedral Mesh Adaptation for CFD Problems, J. Appl. Numerical Mathematics, 26(1-2), 135-151.

Blokkeel, G., Mura, A., Demoulin, F.X., Borghi, R., 2003. A 3D Eulerian Model to Improve the Primary Breakup of Atomizing Jet. SAE paper 2003-01-0005.

Brennen, E.C., 1995. Cavitation and Bubble Dynamics. Oxford University Press.

Chevalier, C., Loussard, P., Muller, U.C., Warnatz, J., 1990. A Detailed Low-Temperature Reaction Mechanism of n-Heptane Auto-Ignition. 2nd Int. Symp. COMODIA 90 Kyoto, p 93.

Dukowicz, J.K., 1980. A Particle-Fluid Numerical-Model for Liquid Sprays. J. Comp. Phys. 35(2), 229-253.

Frenklach, M.,Wang, H., Rabinowitz, M.Y., 1992. Optimization and Analyses of Large Chemical Kinetic Mechanisms Using the Solution Mapping Method-Combustion of Methane. Progress in Energy and Combustion Science, Vol 18, pp 47-73.

Halstead, M., Kirsch, L., Quinn, C., 1977. The Autoignition of Hydrocarbon Fuels at High Temperatures and Pressures- Fitting of a Mathematical Model. Combustion and Flame, Vol 30, pp 45-60.

Hergart, C., Barths, H., and Peters, N., 1999. Modeling the Combustion in a Small-Bore Diesel Engine Using a Method Based on Representative Interactive Flamelets, SAE Paper No. 1999-01-3550.

Hieber, S., 2001. An Investigation of the Mesh Dependence of the Stochastic Droplet Applied to Dense Liquid Spray, Master's Thesis, Mathematics Department,

www.manaraa.com

Michigan Technological University.

Hiroyasu, H. and Nishida, K., 1989. Simplified Three-Dimensional Modeling of Mixture Formation and Combustion in a D.I. Diesel Engine. SAE Paper 890269.

Hountalas, D.T., Kouremenos, A.D., 1998. Development of a Fast and Simple Simulation Model for the Fuel Injection System of Diesel Engines. Advancing in Engineering Software, 29, 13-28.

Huh, K.Y., Gosman, A.D., 1991. A Phenomenological Model of Diesel Spray Atomization. Proceedings of International Conference on Multiphase flow.

Huh, K.Y., Lee, E.J., Koo, J.Y., 1998. Diesel Spray Atomization Model Considering Nozzle Exit Turbulence Conditions. Atomization and Sprays, Vol 8, pp 453-469.

Jasak, H., Gosman, A.D., 2000. Automatic Resolution Control for the Finite Volume Method, Part 2: Adaptive Mesh Refinement and Coarsening, Numerical Heat Transfer, Part. B, 38 (3), 257-271.

Kong, S. C., Senecal, P.K., Reitz, R.D., 1999. Developments in Spray Modeling in Diesel and Direct-Injection Gasoline Engines. Oil & Gas Science and Technology – Rev. IFP, 54 (2), 197-204.

Kong, S. C., Han, Z., Reitz, R.D., 1995. The Development and Application of a Diesel Ignition and Combustion model for Multidimensional Engine Simulation, SAE Paper No. 950278.

Kong, S. C., and Reitz, R. D., 2002. Application of Detailed Chemistry and CFD for predicting Direct Injection HCCI Engine combustion and Emissions, Proc. Combust. Inst., 29, pp. 663-669.

Kong, S. C., Patel, A., Yin, Q., and Reitz, R. D., 2003. Numerical Modeling of Diesel Engine Combustion and Emissions Under HCCI-Like Conditions With High EGR

www.manaraa.com

Levels, SAE Paper No 2003-01-1087.

Kong, S. C., Yong, S., and Reitz, R. D., 2007. Modeling Diesel Spray Flame Liftoff, Sooting Tendency, and NOx Emissions Using Detailed Chemistry With Phenomenological Soot Model. Journal of Eng. For Gas Turbine and Power, Vol. 129, pp. 245-251.

Kuo, K.K., 1986 Principles of Combustion. Wiley, New York, NY.

Libby, P.A., Williams, F.A., 1994. Turbulent Reacting Flows. Acadamic Press, New York, NY.

Lippert, A.M., Chang, S., Are, S., Schmidt, D.P., 2007. Mesh Independence and Adaptive Mesh Refinement for Advanced Engine Spray Simulations. SAE Paper 2005-01-0207.

Nagle, J. and Strickland-Constable, R.F., 1962. Oxidation of Carbon Between 1000-2000 C, Proc. Of the Fifth Carbon Conf., Vol. 1, Pergamon Press, London, p. 154, 1962.

Nishimura, A., Assanis, D.N., 2000. A Model for Primary Diesel Fuel Atomization Based on Cavitation Bubble Collapse Energy. 8th International Conference on Liquid Atomization and Spray Systems, 1249-1256.

Nomura, Y., Miyagawa, H., Taketoshi, T., Tomoda, T., Kubota, M., Abe, S., 2001. Numerical Study of Mixture Formation and Combustion Process in a Direct Injection Gasoline Engine with Fan Shaped Spray. SAE paper 2001-01-0738.

O'Rourke, P.J., Amsden, A.A., 1987. The Tab Method for Numerical Calculation of Spray Droplet breakup. SAE Paper 872089.

Otto, F., Dittrich, P., Wirbeleit, F., 1998. Status of 3D-Simulation of Diesel Combustion. 3rd International Indicating Symp, pp 289-308, Mainz, Germany.

Patterson, M.A., Reitz, R.D., 1998. Modeling the Effect of Fuel Sprays Characteristics on

www.manaraa.com

Diesel Engine Combustion and Emission. SAE paper 980131.

Patterson, M.A., Kong, S.C., Hampson, G.J., Reitz, R.D., 1994. Modeling the Effects of Fuel Injection Characteristics on Diesel Engine Soot and NOx Emissions. SAE paper 940523.

Peters, N., 1984. Laminar Diffusion Flamelet Models in Non-Premixed Turbulent Combustion. Progress in Energy Combustion and Science, Vol. 10,pp 319-339

Peters, N., 1986. Laminar Flamelet concepts in Turbulent Combustion. 21st Symp. Int. Comb, pp 1231-1250.

Peters, N., 1993. Flame Calculation with Reduced Mechanisms – An Outline. In Peters, N., Rogg, B (eds): Reduced Kinetic Mechanism for Applications in Combustion Systems. Lecture Notes in Physics, Springer, Berlin, Germany.

Pickett, L.M., and Siebers, D.L., 2004. Non-Sooting, Low Flame Temperature Mixing-Controlled DI Diesel Combustion. SAE Paper No. 2004-01-1399.

Pickett, L.M., and Siebers, D.L., 2004. Soot in Diesel Fuel Jets: Effects of Ambient Temperature, Ambient Density and Injection Pressure. Combustion and Flame, 138, pp. 114-135.

Reitz, R.D., 1987. Modeling Atomization Process in High Pressure Vaporizing Sprays Atomization and Spray Technology 3, 309-337.

Reitz, R.D., Bracco, F.V., 1982. Mechanism of Atomization of Liquid Jets. The Physics of Fluids, Vol 25, pp 1730-1742

Reitz, R.D., Diwakar, R., 1987. Structure of High Pressure Fuel sprays. SAE paper 870598.

Sarre, C.K., Kong, S.-C., Reitz, R.D., 1999. Modeling the Effects of Injector Nozzle Geometry on Diesel Sprays. SAE Paper 1999-01-0912.

www.manaraa.com

Schmidt, D.P., Rutland, C.J., 2000. A New Collision Algorithm, J. Comp. Phys. 164, 62-80.

Siebers, D.L., 1998. Liquid-Phase Fuel Penetration in Diesel Sprays. SAE Paper, 980809

Stiesch, G., 2004. Modeling Engine Spray and Combustion Process. Springer.

Subramaniam, S., O'Rourke, P.J., 1998. Numerical Convergence of the KIVA-3 Code for Sprays and Its Implications for Modelling, LAUR 98-5465, Los Alamos National Lab, Los Alamos, NM.

Taylor, G.I., 1963. The Instability of Liquid Surfaces when Accelerated in a Direction Perpendicular to their Lanes. In Batchelor, G.K., The Scientific Papers of Sir Taylor, G.I., 3, 532-536.

Torres, D.J., Trujillo, M.F., 2006. KIVA-4: An Unstructured ALE Code for Compressible Gas Flow with Sprays. J. Comp. Phys. 219 (2), 943-975.

Torres, D.J., 2007. Collocated KIVA-4. 11th Int. Multidimensional Engine Modelling User's Group Meeting at the SAE Congress, Detroit, Michigan, April 15th.

Tsui, Y., Pan, Y., 2006. A Pressure Correction Method for Incompressible Flows using Un-Structured Meshes. Numerical Heat Transfer Part B 49, 43-65.

Von Berg, E., Edelbauer, W., Alajbegovic, A., Tatschl, R., 2003. Coupled Calculation of Cavitating Nozzle Flow, Primary Diesel Fuel Break-Up and Spray Formation with an Eulerian Multi-Fluid Model. ICLASS, 2003.

Wan, Y.P., Peters, N., 1997. Application of the Cross-Sectional Average Method to Calculations of the Dense Spray Region in a Diesel Engine. SAE Paper 972866.

Xue, Q., Kong, S.-C., Torres, D.J., Xu, Z., Yi, J., 2008. DISI Spray Modeling using Local Mesh Refinement. SAE Paper 2008-01-0967.

www.manaraa.com

Xue, Q., Kong, S.-C., 2009. Development of Adaptive Mesh Refinement Scheme for Engine Spray Simulations. Computers and Fluids. 38, 939-949.

Yi, Y., Reitz, R.D., 2003. Modeling the Effect of Primary Atomization on Diesel Engine Emissions. SAE Paper 2003-01-1041.

www.manaraa.com